ACS OMEGA

Open Access

http://pubs.acs.org/journal/acsodf

Article

Dual-Action κ-Carrageenan: A Novel Capping Agent and Dopant Source for Enhanced Photocatalytic ZnO Nanoparticles in Azo Dye and Cr(VI) Degradation

Dan Michael A. Asequia, Daisy Jane D. Erjeno, Carlo Kurt F. Osorio, Christine Joy M. Omisol, Renzo Miguel Hisona, Blessy Joy M. Aguinid, Sitti Zayda B. Halun, Joshua B. Zoleta, Roberto M. Malaluan, Arnold C. Alguno, and Arnold A. Lubguban*

Cite This: *ACS Omega* 2025, 10, 9919−9937

Read Online

ACCESS | Metrics & More | Article Recommendations

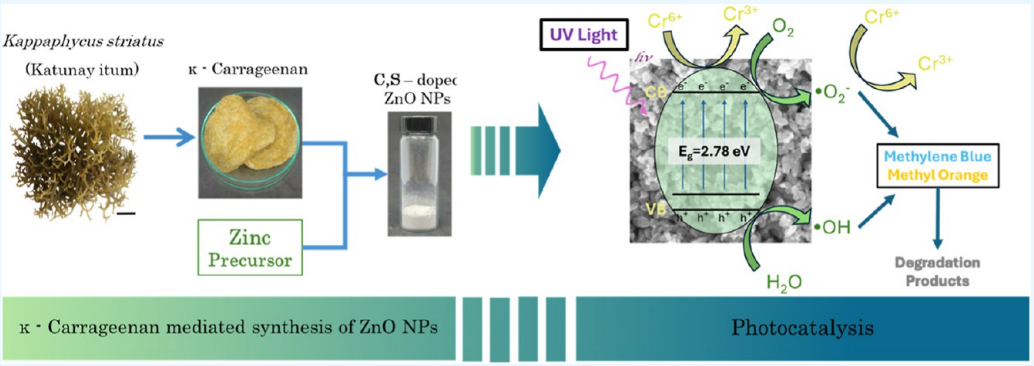

ABSTRACT: Metal oxide nanoparticles synthesized via green routes are increasingly recognized for their potential in water treatment applications due to their enhanced photocatalytic properties. This study presents a novel approach for the synthesis of zinc oxide nanoparticles (ZnO NPs) using κ-carrageenan derived from alkali-treated *Kappaphycus striatus* (Katunay itum) as a capping agent during ZnO NP formation and as a source of nonmetal dopants, carbon, and sulfur. The resulting carrageenan-mediated ZnO NPs (car-ZnO NPs) were thoroughly characterized using physicochemical techniques to evaluate their morphological, optical, and chemical properties. The findings revealed that κ-carrageenan incorporation significantly reduced the band gaps and crystallite sizes of ZnO NPs. Specifically, the 0.75 car-ZnO NPs exhibited the most uniform particle size distribution and demonstrated superior photocatalytic efficiency in degrading methylene blue (MB), methyl orange (MO), and hexavalent chromium (Cr(VI)) under UV light, outperforming unmodified ZnO NPs (0.00 car-ZnO). The enhanced photocatalytic activity is attributed to the narrowed band gap and effective doping with carbon and sulfur, which improved charge carrier separation and extended their lifetime. Additionally, car-ZnO NPs showed excellent photostability and high efficiency in repeated photocatalytic cycles, emphasizing their eco-friendly nature and practicality for water treatment. This study highlights the dual role of κ-carrageenan as a promising, sustainable material for synthesizing ZnO NPs with advanced photocatalytic properties, offering a green alternative for effective wastewater treatment and environmental remediation.

INTRODUCTION

The rapid industrial expansion that has significantly improved living standards has also led to increased pollution levels, particularly in aquatic environments. These environmental domains often receive untreated industrial and household wastewater, which represents the culmination of pollution pathways.[1−3] According to a UN report titled "Partnership and cooperation for water", approximately 44% of untreated domestic wastewater, 70% of untreated industrial wastewater, and 68% of total wastewater flow directly into water sources, undermining progress toward the sustainable development goal of clean water.[4] The most common industrial pollutants discharged into the environment are dyes and heavy metals. Globally, azo dyes such as methylene blue (MB) and methyl orange (MO) account for about 70% of all commercial dyes.[5] These dyes contain hazardous aromatic groups and −N═ N−,

Received: July 1, 2024
Revised: February 21, 2025
Accepted: February 26, 2025
Published: March 4, 2025

which are toxic, teratogenic, and carcinogenic, thus posing significant risks to both the environment and living organisms.[6,7] Additionally, the tanning sector annually employs between 4000 and 6000 tons of basic chromium (Cr), with approximately 20.0 to 40.0% discarded as waste.[2] The hexavalent form of chromium (Cr(VI)) is particularly concerning due to its high water solubility and acute toxicity, with toxicity levels 100 times greater than Cr(III), and is linked to carcinogenic effects.[2,8,9] With this, urgent measures are imperative to preventing their introduction into aquatic ecosystems.

Considerable efforts have been directed toward addressing water pollution, with advanced oxidation processes emerging as a focal point due to their distinctive ability to transform pollutants into harmless substances. Semiconductor-mediated photocatalysis is especially effective for mitigating heavy metals and organic dyes through reduction/oxidation (redox) reactions without generating secondary pollution. Given the pressing concerns about energy shortages, utilizing semiconductors that respond to cost-effective light sources, such as visible and UV light, is crucial.[6,10,11] Zinc oxide nanoparticles (ZnO NPs) represent a prominent example of n-type semiconductors, characterized by a relatively narrow band gap (E_g = 3.38 eV), excellent stability, and strong absorption of visible and UV light, making them widely utilized in the photocatalytic degradation of dyes and heavy metals. However, like many other catalysts, the short lifespan of photoinduced electron−hole (e^-−h^+) pairs significantly limits the performance of ZnO NPs.[8,12−14]

Researchers are currently exploring strategies such as morphological control, doping with metals and nonmetals, and forming heterojunctions to enhance ZnO NPs' efficiency.[13] Among these strategies, nonmetal doping is particularly environmentally friendly due to the use of less harmful dopant precursors. Introducing nonmetal dopants into ZnO creates localized energy levels above the valence band (VB), which effectively narrows the band gap. The formed localized state above the VB acts as hole (h^+) traps that prolong the recombination of photoinduced charge carriers, effectively enhancing the material's photoactivity. Previous reports on nonmetal doping showed a narrowed band gap due to these intermediate localized levels forming above the VB, which delays the recombination of (e^-−h^+) pairs. Furthermore, the introduction of doping materials into the ZnO lattice leads to the formation of point defects. This involves the creation of oxygen vacancies and zinc interstitials caused by the lattice strain induced by the varying ionic radii of the introduced dopants. These defects generate intermediate bands within the forbidden band gap of ZnO.[12−14]

Nonmetal doping on ZnO NPs has been reported in various studies with carbon and nitrogen dopants as dominantly studied materials. Incorporating anionic carbon (C^{4-}) into the ZnO lattice expands its light absorption capacity, accelerates the migration rate of charge carriers, and boosts the photodegradation of contaminants.[12,15] Conversely, sulfur doping in ZnO significantly reduces the band gap of ZnO and improves its optoelectrical characteristics due to the substantial disparity in ionic radius and electronegativity between S and O.[16,17] Co-doping of carbon and sulfur in TiO_2 nanoparticles has been previously reported, with the modification resulting in band gap narrowing and enhanced photocatalytic activity.[18−20] However, to the best of our knowledge, there is no literature on the use of both carbon and sulfur as nonmetal dopants for ZnO NPs.

The development of nonmetal doped ZnO for environmental remediation faces challenges due to the reliance on expensive nonmetal sources, such citric acid,[12] furfural,[21] methylimidazole,[22] and others for carbon doping and sodium sulfide,[23,24] thiourea,[16] and others for sulfur doping, which limits their broader application in photocatalysis. Moreover, the synthesis process for C- or S-doped ZnO often involves multiple steps or the use of harmful chemicals, raising environmental concerns and necessitating expensive equipment and complex process controls.

This study addresses the mentioned gaps by incorporating carbon (C) and sulfur (S) into the crystal lattice of ZnO NPs using carrageenan extracted from *Kappaphycus striatus* (Katunay itum), a biopolymer rich in C and S. Carrageenan serves as a capping and stabilizing agent, regulating the size and improving the morphology of ZnO NPs. Furthermore, various characterization techniques were employed to analyze the phase structure, optical properties, chemical state, and morphology of the synthesized C,S-doped ZnO NPs. These nanoparticles were also assessed for their ability to photodegrade azo dyes (methylene blue and methyl orange in aqueous solutions) and hexavalent chromium, offering a promising green approach to mitigating environmental pollutants in wastewater.

EXPERIMENTAL SECTION

Reagents and Materials. Zinc sulfate heptahydrate [$Zn(SO_4)\cdot 7H_2O$] and potassium dichromate ($K_2Cr_2O_7$) were obtained from HiMedia Laboratories (USA). Sodium hydroxide (NaOH), methylene blue ($C_{16}H_{18}ClN_3S$), and methyl orange ($C_{14}H_{14}N_3NaO_3S$) were sourced from Merck (Germany). Absolute ethanol (C_2H_5OH) and phosphoric acid (H_3PO_4) were purchased from Scharlau (Spain). 1,5−Diphenylcarbazide [$(C_6H_5NHNH)_2CO$] was acquired from Loba Chemie (India), while acetone [$(CH_3)_2CO$] and sulfuric acid (H_2SO_4) were purchased from RCI Labscan (Thailand). All chemicals were of analytical grade and used without further purification. Milli-Q (Type I) water was employed throughout the study. κ-Carrageenan, derived from *K. striatus* (Katunay itum), was sourced from the Niche Centers in the Region (NICER)—Seaweed Research and Development Center at Mindanao State University—Tawi-Tawi, located in Sanga-Sanga, Bongao, Tawi-Tawi, Philippines. For the κ-carrageenan supplied for this study, the center used the alkali-extraction method using KOH, as outlined by Villanueva et al.[25] For photocatalytic reactions, a reactor with 352 nm UV light (five 8 W lamps connected in parallel) was used for UV irradiation of the reaction mixture.

Synthesis of ZnO NPs Using κ-Carrageenan. The synthesis of ZnO nanoparticles was carried out by mixing 50 mL of 0.25 M zinc sulfate heptahydrate solution, used as a precursor, with varying concentrations of 50 mL of aqueous carrageenan extracts (0.00% w/v, 0.25% w/v, 0.50% w/v, 0.75% w/v, and 1.00% w/v). A 50 mL volume of 0.50 M NaOH solution was added dropwise. The solution was vigorously mixed at 80 °C for 2 h. The mixture was then aged for 18 h. After being aged, the precipitate was centrifuged and subsequently washed with water and ethanol. The washed samples were dried in an oven at 80 °C overnight and annealed in a muffle furnace for 2 h at 500 °C. Characterization studies were carried out after the annealed samples were recovered.

https://doi.org/10.1021/acsomega.4c06074
ACS Omega 2025, 10, 9919−9937

Scheme 1. Schematic Diagram of the Synthesis of ZnO NPs Using κ-Carrageenan

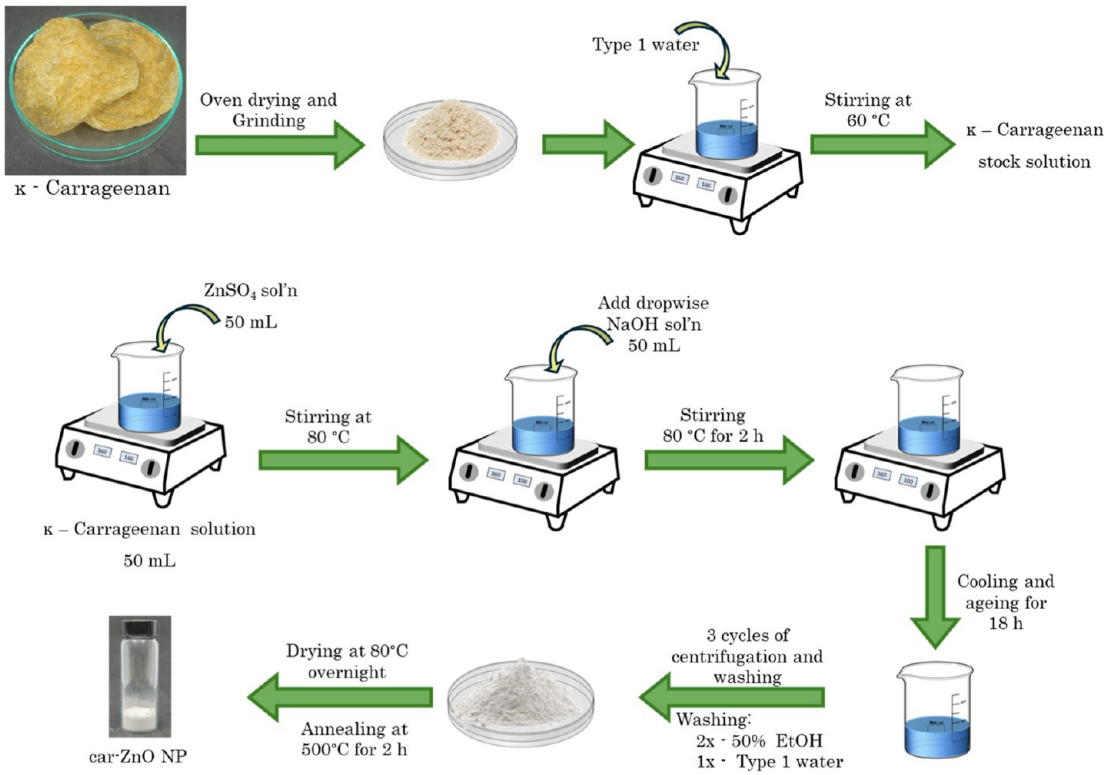

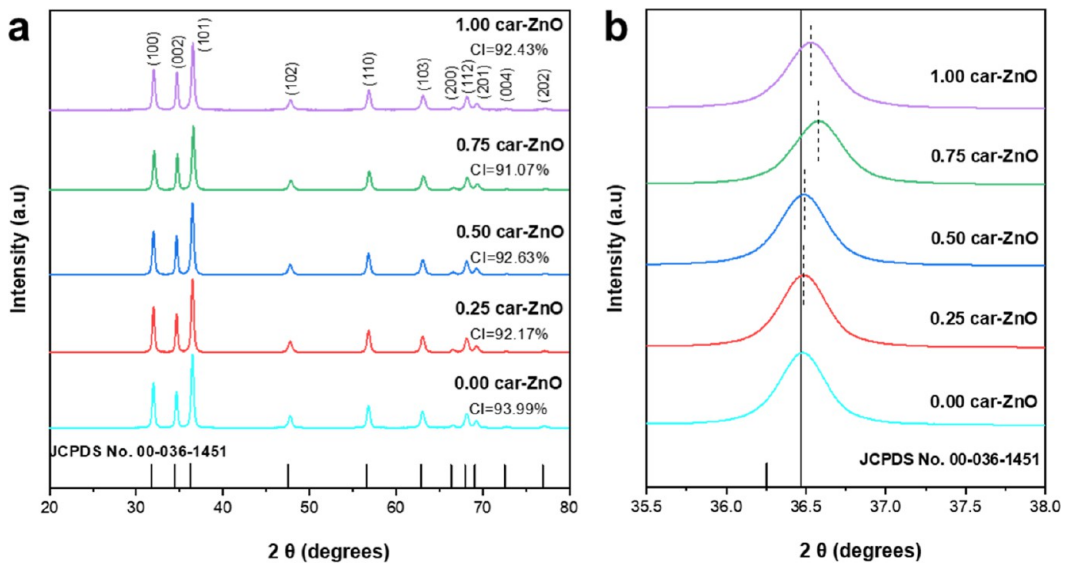

Figure 1. (a) XRD patterns of annealed ZnO NPs samples. (b) Shifting of (101) peaks of different ZnO NPs samples.

Scheme 1 provides a schematic summary of the car-ZnO NP synthesis.

Instrumentation. X-ray diffraction (XRD) patterns were obtained using a Shimadzu XRD MAXima 7000 (Japan) with Cu Kα radiation (λ = 1.5406 Å), operating at 40 kV and 30 mA. The measurements were conducted over an angular range of 3° to 90° 2θ with a scanning speed of 0.02° 2θ per 0.60 s. Scanning electron microscopy (SEM) was employed to examine the morphology, shape, and purity of the nanoparticles using a JEOL JSM-IT210 microscope equipped with an energy-dispersive X-ray (EDX) attachment (Japan). SEM images were captured with a secondary electron detector under high vacuum conditions, applying an accelerating voltage of 15 kV and a magnification of ×30,000. Transmission electron microscopy (TEM) was performed using a JEOL JEM 2100 Plus LaB6 TEM with STEM (Japan) to analyze the morphology, size, and selected area electron diffraction (SAED) pattern of the 0.75 car-ZnO NPs.

Fourier transform infrared (FT-IR) spectroscopy was employed to determine the surface functionality of various ZnO nanoparticles. The spectra were recorded in the range of 400−4000 cm^{-1} using a Shimadzu ATR−FTIR IRTracer-100 spectrometer (Japan). X-ray photoelectron spectroscopy (XPS) was conducted by using a JEOL JPS-9200 spectrometer

https://doi.org/10.1021/acsomega.4c06074
ACS Omega 2025, 10, 9919−9937

(Japan), equipped with a monochromatized Al Kα X-ray source operating at 100 W under ultrahigh vacuum conditions ($\sim 10^{-7}$ Pa). The narrow scan spectra for Zn 2p, O 1s, C 1s, and S 2p were obtained and calibrated using the binding energy of adventitious carbon at 285.0 eV.

The UV−Vis absorption spectrum of the ZnO nanoparticles was recorded using a Thermo Scientific GENSYS 10S UV−Vis spectrophotometer (USA) over the wavelength range of 200−550 nm. Measurements were carried out in quartz cuvettes with Type I water used as the reference solvent.

Photocatalytic Study. The photocatalytic activity of ZnO on different staining dyes, namely, methylene blue (MB) and methyl orange (MO) and heavy metal Cr(VI), was carried out using UV irradiation in the photocatalytic reactor. The removal of pollutants from aqueous solution by photocatalytic degradation depends on the amount of ZnO loading, pollutant concentration, and pH and the different synthesized car-ZnO NPs. Before irradiation, the suspensions were stirred for 30 min in the dark to achieve an adsorption/desorption equilibrium. A 5 mL sample of the suspension was taken out at different time intervals and centrifuged at 4500 rpm for 10 min, and the UV−vis absorption spectrum was recorded. For the determination of hexavalent chromium, colorimetric carbazide assay is performed.[26] The photodegradation of MB, MO, and Cr(VI) solutions was determined using the equation

$$\%\ \text{of photodegradation} = \left(\frac{C_o - C_f}{C_o}\right) \times 100 \quad (1)$$

where C_o and C_f are the initial and final concentrations of Cr(VI) or individual dye solutions, respectively.

RESULTS AND DISCUSSION

Characterization of car-ZnO NPs. *XRD Pattern Analysis.* Various characterizations were conducted to explore how the carrageenan extract affected both the physical and the chemical attributes of the nanoparticles. XRD was utilized to determine the crystal phases present in the annealed nanoparticles. The resulting XRD patterns of the samples provide insight into the crystallinity and crystallite size of the nanoparticle. Figure 1 illustrates distinct peaks in the XRD spectra of all samples, indicating a high level of crystallization. Using the XRD spectra of the control sample (0.00 car-ZnO), the presence of significant peaks at 31.98°, 34.64°, 36.48°, 47.77°, 56.82°, 63.08°, 66.61°, 68.16°, 69.28°, 72.77°, and 77.14° in Figure 1a corresponds to the Miller−Bravais indices of (100), (002), (101), (102), (110), (103), (200), (112), (201), (004), and (202), respectively. Only a slight shift from these significant peaks is observed for the other ZnO NPs samples. The detected diffraction peaks closely match those of the Joint Committee on Powder Diffraction Standards (JCPDS, card No. 36-1451) pattern of ZnO, confirming the hexagonal wurtzite crystal structure of the ZnO NPs. In addition, there are no additional peaks detected in the XRD patterns of all samples, suggesting its significantly pure nature.

A detailed inspection of the enlarged primary (101) peak (Figure 1b) reveals a minor displacement toward higher 2θ values, particularly evident in samples with 0.75% and 1.00% carrageenan loading, where the presence of C and S doping is pronounced. This observation can be attributed to the lattice expansion. Upon meticulous examination of the XRD pattern in Figure 1b, it is evident that the incorporation of C and S has caused a noticeable shift in the (101) plane to higher 2θ values, thereby inducing distortion in the unit cell structure of the material. The impact of C and S doping extends to the alteration of the lattice parameters in car-ZnO, attributable to structural defects (O_{vac}) induced by C and S doping. The larger atomic radii of carbon (C^{4-}) (260 pm) and sulfur (S^{2-}) (184 pm) compared to oxygen (O^{2-}) (140 pm) disrupt the lattice of car-ZnO, promoting the formation of O_{vac} sites.[17,27] Additionally, the substitution of O^{2-} by C^{4-} or S^{2-} results in charge imbalance, necessitating oxygen loss to maintain charge neutrality.[12] The presence of C and S was further confirmed by the XPS and EDX results.

Table 1 outlines the mean crystallite dimensions of the synthesized ZnO NPs computed through the Debye−Scherrer formula[28]

$$D = \frac{0.9\lambda}{\beta_{hkl}\cos\theta} \quad (2)$$

where λ is the Cu K_α radiation wavelength (λ = 0.15406 nm = 1.5406 Å); θ is the diffraction angle in radians; and β_{hkl} is the full width at half-maximum (fwhm) of the corresponding peak. The reduction in the crystallite size of car-ZnO can be attributed to the inclusion of carrageenan extract, serving a dual purpose: inhibiting grain growth and facilitating improved dispersion of the nanoparticles. Further details regarding the dimensions of the ZnO NPs, particularly their particle sizes, are elaborated upon in the SEM and TEM sections.

The interplanar spacing d_{hkl}, the lattice parameters (a and c), and the unit cell volume (V) of a hexagonal system of the samples having the hexagonal wurtzite configuration are determined using the equation outlined below:[8,28] The values of lattice parameters a and c can be computed from the reflections corresponding to the (100) and (002) planes, respectively.

$$d_{hkl} = \frac{n\lambda}{2\sin\theta} \quad (3)$$

$$\frac{1}{d_{hkl}^2} = \frac{4}{3} \times \frac{(h^2 + hk + k^2)}{a^2} + \frac{l^2}{c^2} \quad (4)$$

$$V = 0.866 \times a^2 \times c \quad (5)$$

The determined lattice constants and their associated unit cell volumes are listed in Table 1. It is noticeable that the lattice parameters of car-ZnO nanoparticles are marginally reduced in comparison to unmodified ZnO, suggesting the imposition of constraints induced by the dopants.

The synthesized ZnO NPs exhibit a hexagonal wurtzite structure, wherein tetrahedrally coordinated O^{2-} and Zn^{2+} ions alternately stack along the c axis. This arrangement creates a noncentrally symmetric structure, leading to the formation of polar surfaces within the lattice. Specifically, the polarity is primarily located on the basal planes, with positively charged Zn−(0001) and negatively charged O−(000$\bar{1}$).[29,30] Structurally, ZnO features three principal fast growth directions: $\langle 2\bar{1}\bar{1}0\rangle$ ($\pm[2\bar{1}\bar{1}0]$, $\pm[\bar{1}2\bar{1}0]$, $\pm[1\bar{1}20]$); $\langle 01\bar{1}0\rangle$ ($\pm[01\bar{1}0]$, $\pm[10\bar{1}0]$, $\pm[1\bar{1}00]$); and $\pm[0001]$.[30] At the initial growth phase, κ-carrageenan attached to the positively charged plane (along the c axis) of the ZnO hence hindering its growth along this direction. Upon annealing the samples, the site where κ-carrageenan is richly present, i.e., along the c axis, is probably the most active site where atom rearrangement is prevalent.

https://doi.org/10.1021/acsomega.4c06074
ACS Omega 2025, 10, 9919−9937

Table 1. Summary Data of Crystallite Size and Crystallinity Index via XRD Results and Optical Properties from UV−Vis Spectra of Different car-ZnO NPs

sample	average crystallite size D (nm)	crystallite size at Miller−Bravais indices (101) peak			lattice parameters (Å)		unit cell volume (Å)^3	crystallinity index (%)	UV−vis absorption peak (nm)	band gap (eV)
			d_{100}	d_{002}	$a = b$	c				
0.00 car-ZnO NP	18.08	21.66	2.796	2.588	3.228	5.175	46.712	93.99	373	3.09
0.25 car-ZnO NP	17.88	21.61	2.795	2.587	3.228	5.174	46.699	92.17	374	3.04
0.50 car-ZnO NP	17.10	20.66	2.795	2.587	3.228	5.174	46.702	92.63	374	3.00
0.75 car-ZnO NP	16.80	19.89	2.787	2.580	3.218	5.160	46.580	91.07	377	2.78
1.00 car-ZnO NP	16.94	20.20	2.791	2.584	3.223	5.167	46.643	91.07	375	2.89

Table 1 shows that the c axis has a more significant change in the lattice parameters, suggesting huge distortion along this axis. Although the ionic radius of C and S is bigger compared to O, the replacement of O^{2-} by C^{4-} or S^{2-} results in charge imbalance, necessitating oxygen loss to maintain charge neutrality. The presence of these O_{vac} molecules along the c axis resulted in a decrease in the c lattice parameter.

UV−Visible Spectral Analysis. The light absorption and direct band gap of car-ZnO NPs were examined using UV−vis spectroscopy analysis by assessing the UV−vis spectra of the ZnO NPs aqueous dispersed solution within the range of 200 to 550 nm. Figure 2a illustrates the UV−vis absorption spectra of the car-ZnO nanoparticles, revealing a prominent peak within the 300−400 nm range, indicative of the characteristic attributes of ZnO nanoparticles.[31] The corresponding peaks for each sample are listed in Table 1. The Tauc plot method is employed to determine the optical band gap of each synthesized ZnO nanoparticle, as depicted in Figure 2b. To obtain the absorption coefficient of each sample, the following equation is applied

$$E_g = (h\nu) - \alpha h\nu^2 \tag{6}$$

where α is the absorption coefficient, $h\upsilon$ is the photon energy, and E_g is the optical band gap energy. The band gap energies of car-ZnO NPs are listed in Table 1.

It is evident that the synthesized car-ZnO NPs exhibit lower E_g values than the unmodified ZnO NP (0.00 car-ZnO). The narrowing of the band gap energy can be attributed to the presence of the introduced nonmetal (C,S) dopants derived from thermally degraded products of κ-carrageenan. These data findings align with previous studies demonstrating the decrease in E_g of ZnO NPs with the introduction of nonmetal dopants C and S. Most notably, the reduction in E_g of the ZnO NPs offers an advantageous influence on the photocatalytic potency of this material apropos of its intended purpose.[12] Moreover, it is noted that there exists an inverse relationship between E_g and κ-carrageenan concentration, where E_g decreased from 3.09 to 2.78 eV as the κ-carrageenan concentration increased from 0.00% to 0.75%. However, with a further increase in the κ-carrageenan concentration to 1.00%, there is a slight rise in the band gap energy. This trend could be attributed to the potential saturation point reached at 0.75% κ-carrageenan concentration. With the subsequent addition of nonmetal dopants, formation of localized states above the VB narrows down the band gap of ZnO. Furthermore, doping ZnO introduces point defects, such as oxygen and zinc vacancies, due to the lattice expansion produced by the large ionic radius of the dopants, which give rise to broadened localized bands above the VB of ZnO.[12,15,16]

FTIR Spectral Analysis. Fourier transform infrared (FTIR) spectroscopy was conducted to identify the surface functionalities of the synthesized ZnO NPs. In Figure 3b, a prominent absorption band at around 419 cm^{-1} was detected and assigned to the Zn−O stretching signal. Figure 3a shows absorption bands at 3,314 cm^{-1}, 2,361 cm^{-1}, 1,643 cm^{-1}, and 1,527 cm^{-1}, which correspond to the stretching vibration of O−H in H_2O, the O═C═O bending vibration of CO_2 in air, the C═O bond vibrations, and O−H stretching vibration of surface hydroxyl bonds.[32−34] The absorption peaks at 2,949 and 2,926 cm^{-1}, and 1,742 cm^{-1} is assigned to C−H stretching and C═O stretching from conjugated anhydride. The absorption bands at 1,328 cm^{-1}, 1,137 cm^{-1}, and 919 cm^{-1}

https://doi.org/10.1021/acsomega.4c06074
ACS Omega 2025, 10, 9919−9937

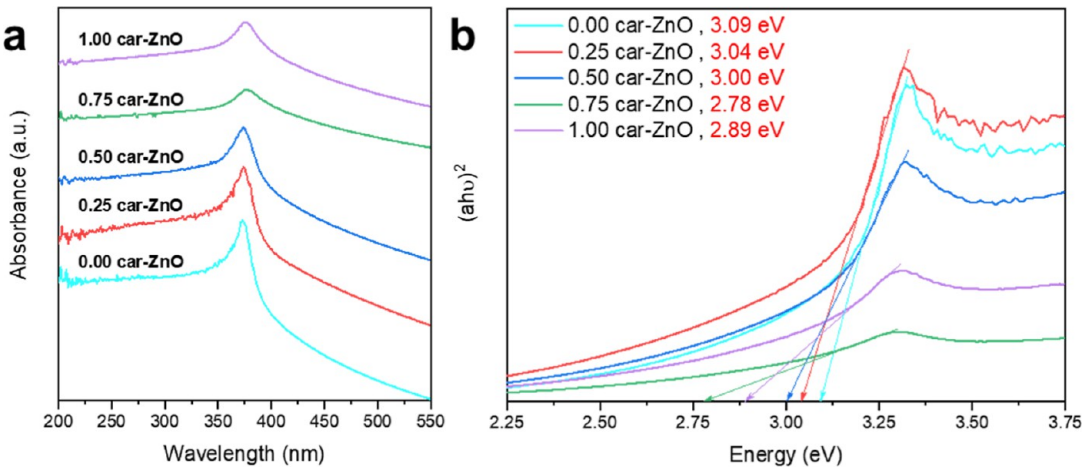

Figure 2. (a) UV−vis absorption spectra and (b) band gap energy calculated using the Tauc plot of different car-ZnO NPs.

are attributed to the C−O asymmetric stretching of the carboxylate group, the C−O symmetric bond stretch, and the out-of-plane polarized C−O stretch.[34−36] It is noteworthy that in the FTIR spectra of car-ZnO samples, the absorption peaks observed at 1,328 cm^{-1}, 1,137 cm^{-1}, and 919 cm^{-1} can be attributed to the asymmetric stretching frequency of S═O bonds, symmetric S−O stretching, and asymmetric S−O stretching.[37,38] The presence of carbon and sulfur groups serves as preliminary evidence of nonmetal doping within the nanoparticles. Notably, the intensity of the carbonyl group (C═O) increases proportionally with the concentration of carrageenan. Conversely, the detection of sulfur groups in the FTIR spectra is not conclusive evidence of successful S doping given the relatively low sulfur content in carrageenan compared to carbon. Therefore, further validation through XPS analysis was done to confirm the successful incorporation of sulfur dopants and provide further verification of C doping.

In Figure 3c, the absorption peaks at 1,638 cm^{-1} and 1262 cm^{-1} correspond to polymer-bound water and the asymmetric stretching of O═S═O, respectively.[39,40] A broad peak ranging from 1178 to 782 cm^{-1} was observed in the as-prepared 0.75 car-ZnO NP, which can be divided into four peaks: the absorption peak at 1,083 cm^{-1} is assigned to glycosidic linkage, the peak at 970 cm^{-1} to 3,6-anhydro-D-galactose, the absorption peak at 896 cm^{-1} to the C_6 group in β-D-galactose, and 845 cm^{-1} to C_4−O−S sulfate ester bonding in galactose.[40,41] The presence of these peaks along with the peak at 419 cm^{-1} (Figure 3b) for the as-prepared 0.75 car-ZnO NP confirms the successful capping of ZnO NPs with carrageenan.

XPS Analysis. XPS analysis was conducted to assess the composition and chemical state of both unmodified and carrageenan-mediated ZnO nanoparticles with the findings presented in Figure 4. The primary elements identified through the wide survey spectrum include Zn, O, S, and C, as shown in Figure 4a. In the narrow scan of the Zn 2p spectrum, illustrated in Figure 4b, two bands are observed at approximately 1045 and 1022 eV, corresponding to Zn $2p_{1/2}$ and Zn $2p_{3/2}$, respectively, in the hexagonal wurtzite ZnO form.[42,43] The O 1s XPS peak, shown in Figure 4c, can be deconvoluted into three components at ∼529, ∼531, and ∼533 eV. The band at ∼529 eV is attributed to O^{2-} ions in the Zn−O bonds of wurtzite ZnO crystals (O_I), while the middle binding energy component is linked to oxy-carbon clusters (O_{II}), and the last component can be associated with chemisorbed oxygen (O_{III}), possibly originating from hydroxyl species formed on the surface of the ZnO lattice. Figure 4d depicts three deconvoluted peaks observed in the C 1s XPS spectra, centered approximately at ∼284, ∼286, and ∼288 eV, indicating the presence of carbon in the samples. The peak (C_I) around ∼284 eV is attributed to the elemental carbon (C−C) bond of free carbon,[44] which may arise from carbon contamination during sample preparation, unreacted carbon from precursor materials, or thermal decomposition during annealing, while the peak (C_{II}) near ∼286 eV is associated with the substitutional doping of carbon in the ZnO lattice (Zn−O−C).[15,34,45] The final peak (C_{III}), situated around ∼288 eV, is attributed to carboxyl carbon (O−C═O) or carbon integrated into the interstitial sites of the ZnO.[42,45] The intensity of C_{II} shows a notable increasing trend as the concentration of the carrageenan extract rises, suggesting that higher amounts of carrageenan facilitate greater incorporation of carbon into the ZnO structure. This enhanced substitutional doping may result from the increased availability of reactive sites provided by the carrageenan before annealing, which promotes carbon integration into the lattice upon thermal decomposition. In contrast, the intensity of C_I generally decreases with increasing carrageenan extract concentration, highlighting that the additional carrageenan enhances bonding with the ZnO matrix and minimizes unreacted or free carbon, which can negatively impact the material's properties. However, the trend of C_I necessitates further exploration, as its complex interaction with the carbon source—whether arising from environmental contamination or the carrageenan itself—needs to be better understood. Interestingly, the peak corresponding to C_{III} does not show any discernible trend with varying concentrations of carrageenan. This lack of trend may indicate a stable presence of carboxyl groups or suggest that synthesis conditions limit the influence of the carrageenan concentration on this specific carbon environment.

The binding energy shifts observed in the C 1s XPS spectra provide insights into the interactions of carbon species within the synthesized ZnO nanoparticles. The C_I around ∼284 eV shows minimal shifts, indicating stable interactions between carbon and the ZnO matrix, suggesting that as the carrageenan concentration increases, free carbon formation diminishes. Similarly, the C_{II} peak at ∼286 eV experiences slight shifts to higher binding energy with increased carrageenan concen-

https://doi.org/10.1021/acsomega.4c06074
ACS Omega 2025, 10, 9919−9937

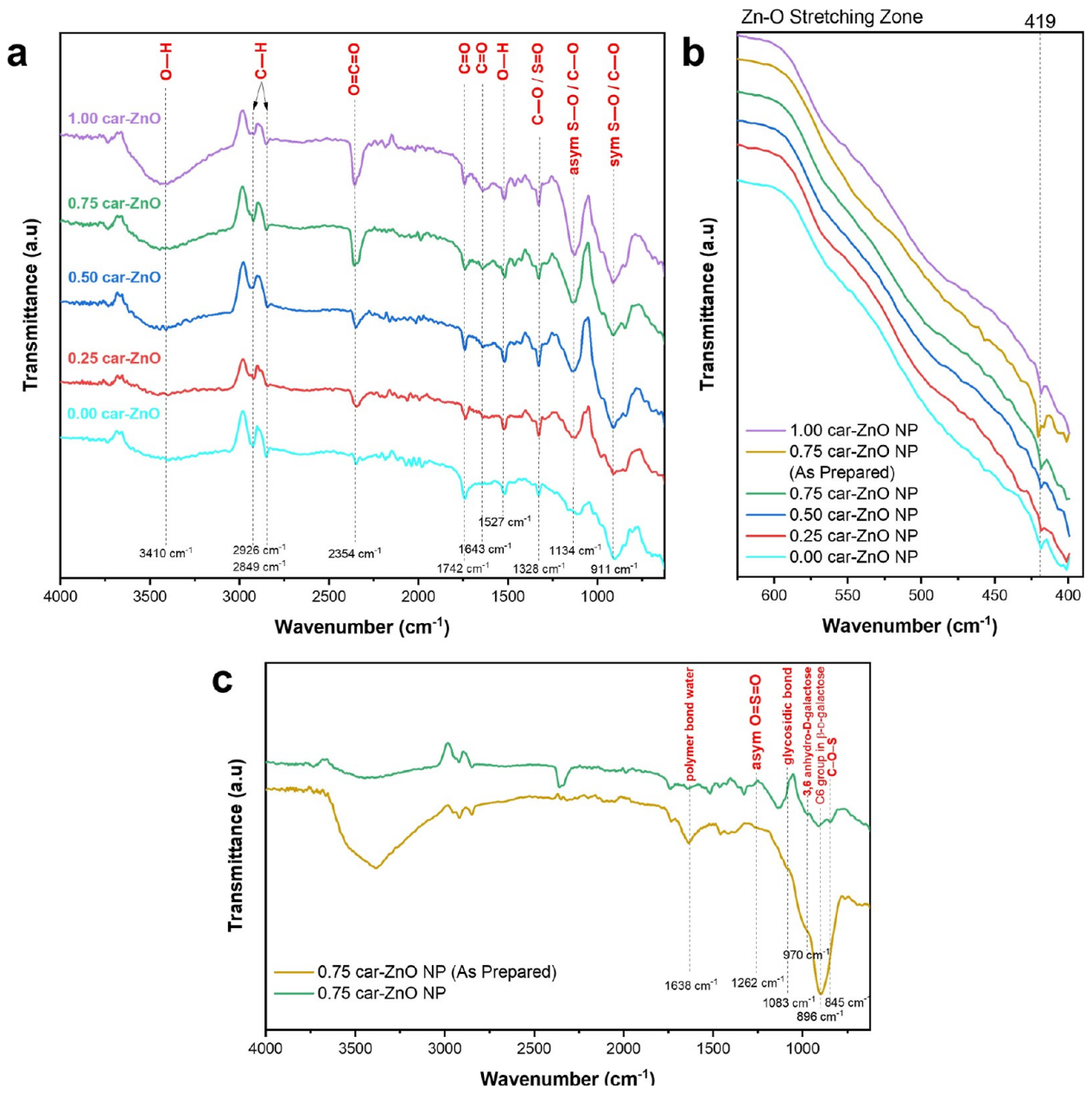

Figure 3. FTIR spectra of ca. different ZnO NPs synthesized with different carrageenan concentrations: (a) 4000−625 cm^{-1} and (b) 625−375 cm^{-1} and (c) comparison of 0.75 car-ZnO NP before and after annealing.

tration, reflecting enhanced bonding interactions without significant alterations to the electronic environment. The C_{III} peak at around ∼288 eV also exhibits minimal shifts, indicating a stable presence of carboxyl groups or interstitial carbon across different carrageenan concentrations. Overall, the minimal binding energy shifts highlight the stable carbon−ZnO interactions, underscoring the consistent chemical states of carbon in the synthesized nanoparticles.

The binding energies at ∼163 eV and ∼164 eV in Figure 4e correspond to the $2p_{3/2}$ and $2p_{1/2}$ states of the lower valence state of S^{2-}. Meanwhile, the peaks observed at ∼167 eV and ∼168 eV originate from the S^{6+} $2p_{1/2}$ and $2p_{3/2}$ states, respectively, indicating that sulfur exists in its highest oxidation state (+6).[46,47] The appearance of the C 1s and S 2p peaks further confirms the successful doping of ZnO NPs with nonmetal dopants, in which the main contributor to the doping effect is carbon due to its higher intensity compared to sulfur peaks on the wide survey scan which is in good agreement with the EDS result where carbon is relatively abundant.

Electron Microscopy, SAED Pattern, and EDX Analysis. SEM was utilized to examine the morphology and microstructure of car-ZnO NPs, contrasting them with the unmodified sample. As depicted in Figure 5a−e, well-distributed rice-grain-shaped ZnO NPs of varying sizes, ranging from 40 to 160 nm, were obtained under optimized synthesis conditions, with minimal agglomeration. Further insights into particle organization, dispersion, and distribution of the synthesized ZnO nanoparticles were obtained through TEM analysis. Figure 6a−b displays TEM images of 0.75 car-ZnO nanoparticles (NPs), while Figure 6c−d illustrates their size distribution, showing mean diameters of 33.59 nm and lengths of 67.62 nm. These findings corroborate previous assertions on the size and shape of the synthesized NPs.

https://doi.org/10.1021/acsomega.4c06074
ACS Omega 2025, 10, 9919−9937

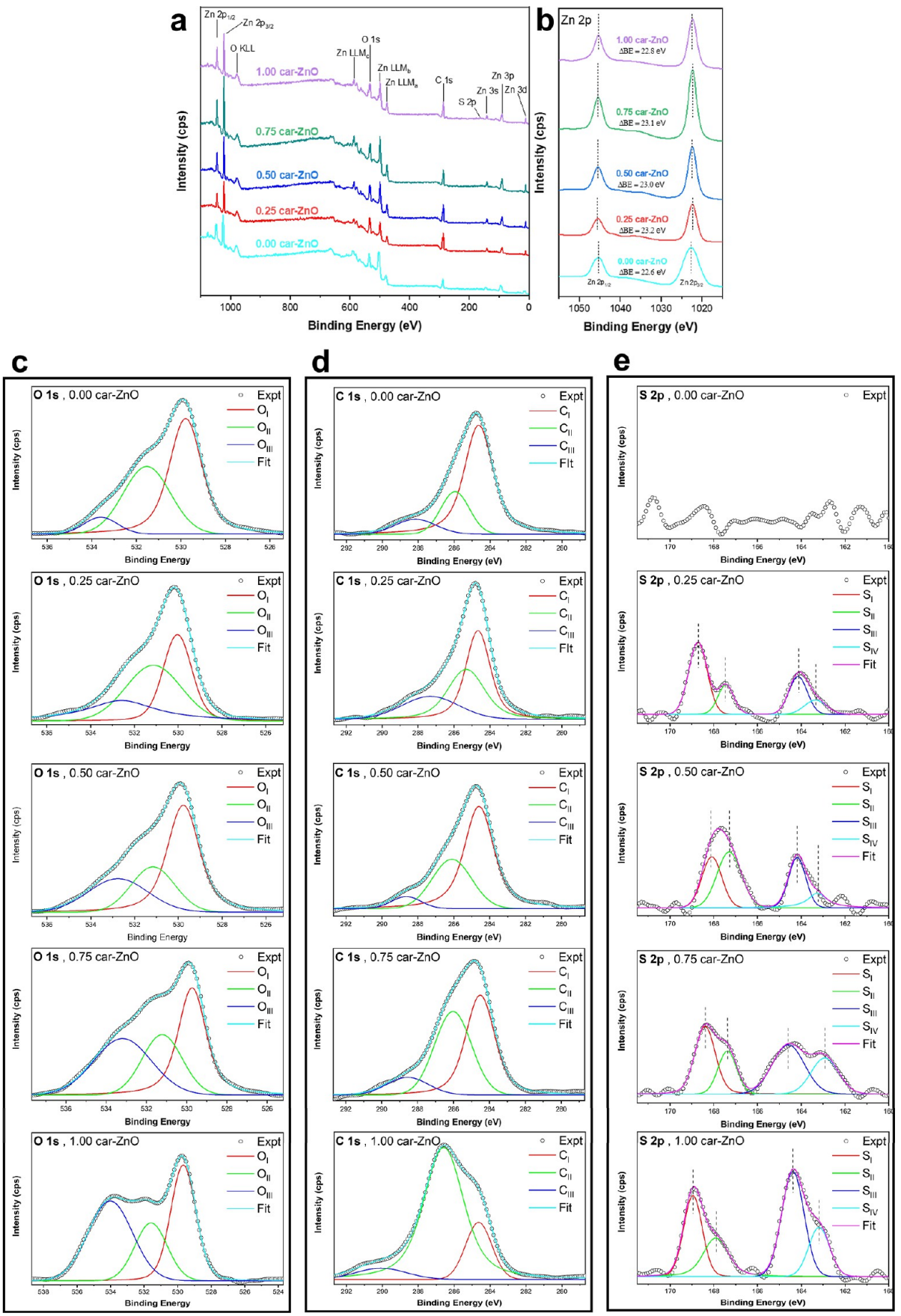

Figure 4. XPS spectra of car-ZnO NPs: (a) survey scan, (b) Zn 2p, (c) O 1s, (d) C 1s, and (e) S 2p.

https://doi.org/10.1021/acsomega.4c06074
ACS Omega 2025, 10, 9919−9937

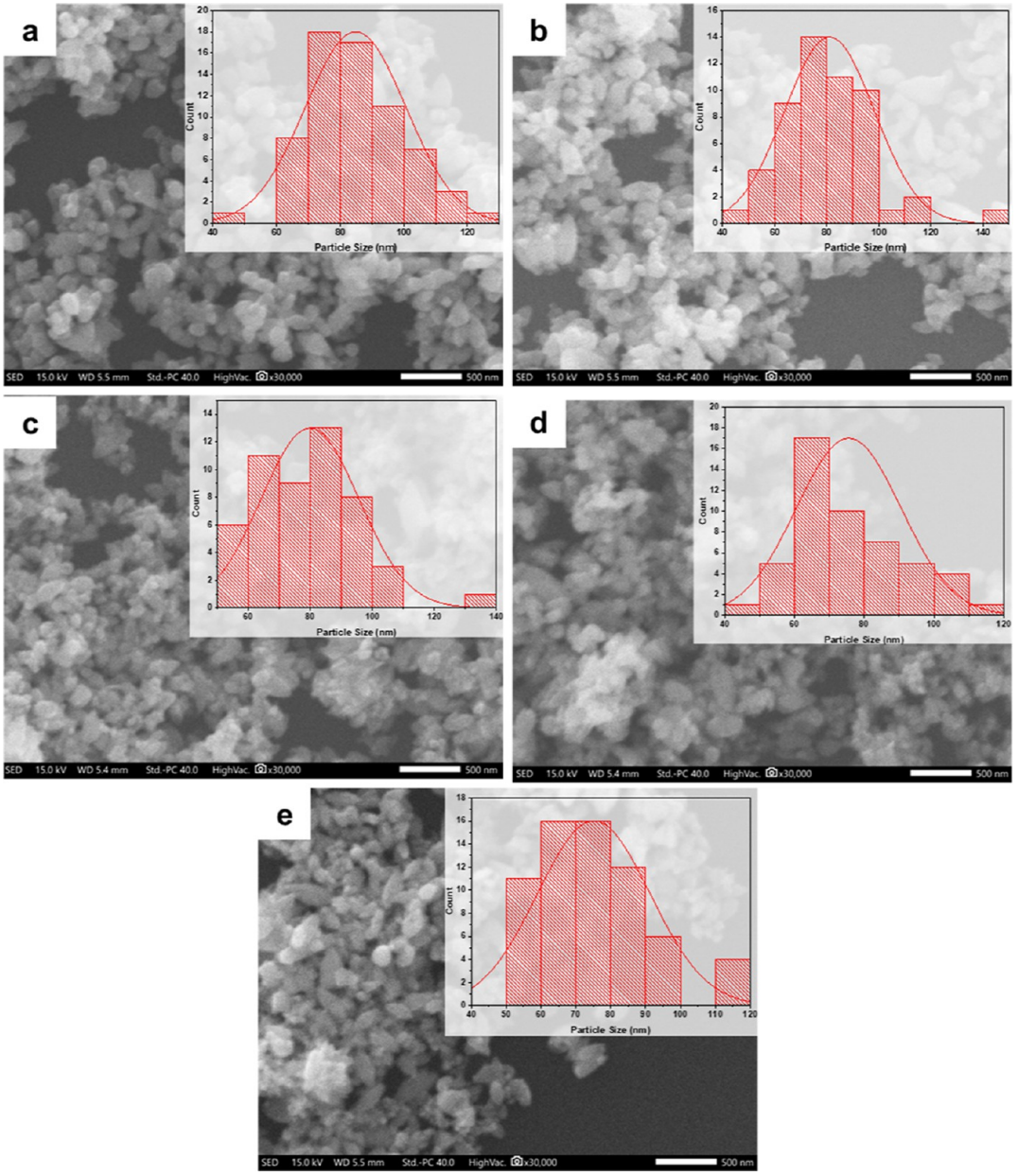

Figure 5. SEM images of ZnO NPs synthesized with different carrageenan concentrations: (a) 0.00%, (b) 0.25%, (c) 0.50%, (d) 0.75%, and (e) 1.00%.

Moreover, the detailed observations on the SAED pattern in Figure 6e corroborate with the XRD findings, confirming the consistent hexagonal wurtzite structure of the synthesized ZnO NPs. Table 2 presents the estimated *d*-spacing values obtained from the SAED pattern, and their corresponding indices matched with the XRD data. Evidently, particle diameter measurements obtained from TEM and SEM techniques are more suitable than XRD pattern analysis, as the former directly determines particle size, while the latter assesses crystal size, contingent on particle shape. Despite the different inferences derived from said tests, a significant consistency in the findings can be noted that supports the posited effects of the active sites carrageenan in reducing zinc(II) cations and capping of freshly formed ZnO NPs resulting to a uniform and hindered growth of particles as supported with the decrease in crystallite size in the XRD results.

The purity of the ZnO NPs was assessed through EDX spectroscopy. EDX spectra (Figure 7) reveal oxygen and zinc peaks, which relate to highly pure ZnO NPs. Trace amounts of carbon and sulfur peaks confirm the successful doping of C and S in synthesized nanoparticles. The silicon and gold peaks present in the spectra are due to the substrate and sputter coating material, respectively, that are used during the sample preparation procedure. Nevertheless, the EDX results coincide with the XRD results on the basis of purity. It is noticeable that the sulfur peaks are absent in the EDX spectra for the 0.25 and 0.50 car-ZnO samples. This absence is likely due to the low concentration of sulfur as a dopant, resulting in a signal that is too weak to be detected in the background noise. Additionally, EDX analyzes a larger volume of the material, which can dilute the signal from trace elements like sulfur. In contrast, XPS, with its higher sensitivity and surface-specific analysis, is capable of detecting low concentrations of sulfur effectively,

https://doi.org/10.1021/acsomega.4c06074
ACS Omega 2025, 10, 9919−9937

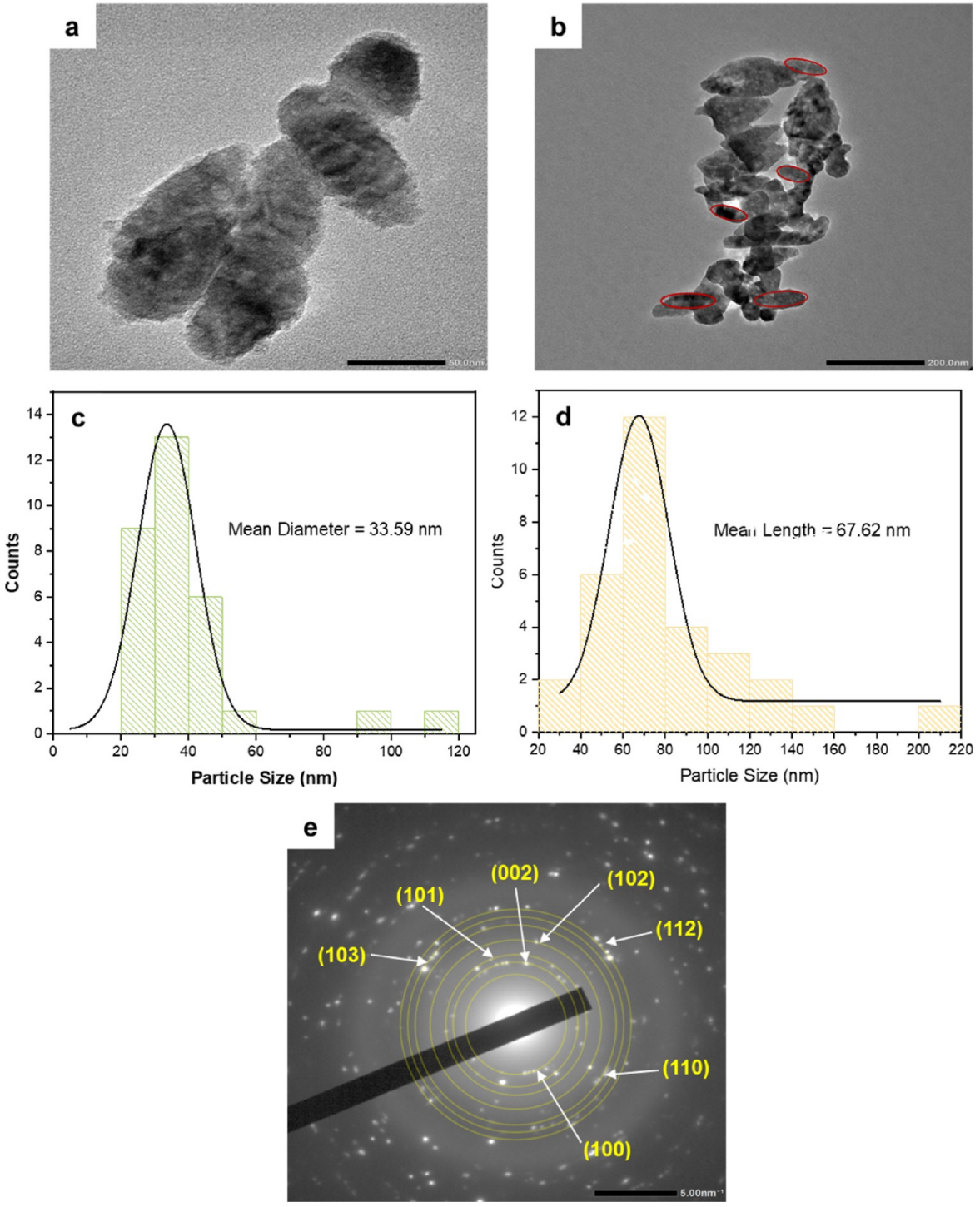

Figure 6. Transmission electron microscope images of 0.75 car-ZnO NP at different measurement scales: (a) 50.0 nm and (b) 200 nm; (c–d) size distribution and (e) SAED pattern.

thus providing a more accurate representation of its presence in the samples. On the other hand, a carbon peak was observed in the control sample (0.00 car-ZnO), despite the absence of an intentional carbon source. This peak is attributed to baseline contamination, likely from environmental factors or sample preparation. Consequently, this baseline measurement can serve as a reference for quantifying and analyzing carbon in other samples where carbon is known to be present.

Proposed Mechanism of κ-Carrageenan-Mediated ZnO NPs Synthesis. Three main processes are involved in the synthesis of C,S-doped ZnO NPs, i.e., reduction, growth, and stabilization. Figure 8 outlines the postulated synthesis pathway of C,S-doped ZnO NPs accordingly derived from the experimental results presented thus far. First, Zn^{2+} ions (blue circles) are dissociated in a solution of κ-carrageenan, depositing the zinc ions into the biopolymer complex. The sulfur-containing groups on the kappa carrageenan facilitate the attraction of Zn^{2+} ions from the solution, allowing the attachment of zinc ions to the sulfate (SO_4^-) functional groups present in the biopolymer network. The hydroxyl (OH^-)

https://doi.org/10.1021/acsomega.4c06074
ACS Omega 2025, 10, 9919−9937

Table 2. Measured Interplanar Spacing (d_{hkl}) Obtained from SAED and XRD Patterns

Miller index (hkl)	d spacing from SAED pattern	d spacing from XRD pattern	standard data (JCPDS no. 00−036−1451)
1 0 0	2.8145	2.7871	2.8143
0 0 2	2.6038	2.5802	2.6033
1 0 1	2.4486	2.4548	2.4759
1 0 2	1.9164	1.8990	1.9111
1 1 0	1.6256	1.6167	1.6247
1 0 3	1.4789	1.4708	1.4771
2 0 0		1.4004	1.4072
1 1 2	1.3795	1.3732	1.3782
2 0 1		1.3536	1.3583
0 0 4		1.2975	1.3017
2 0 2		1.2342	1.2380

groups from the added NaOH aid in the reduction process by contributing electrons, leading to the conversion of zinc ions from a (+2) oxidation state to a zerovalent state. This is subsequently followed by the nucleation of the reduced zinc atoms. Subsequently, ZnO will enter its growth phase where the spontaneous combination of small ZnO NPs into larger NPs occurs through Ostwald ripening, driven by stronger binding energy between Zn metal atoms. This occurrence boosts the thermodynamic stability of zinc nanoparticles. Subsequently, the synthesis progresses to its final stage, stabilization, during which the nanoparticles adopt their most energetically favorable configuration, significantly influenced by κ-carrageenan's capacity to stabilize the metal oxide nanoparticles. The biopolymer effectively caps the ZnO NPs, inhibiting further growth. Through subsequent drying and annealing, the combustion of the organic substance (carrageenan) primarily leaves behind residual carbon and sulfur. At this high-temperature environment, rearrangement of (Zn, C, S, and O) atoms occurs, which eventually results in the substitution of a fraction of oxygen atoms in the ZnO lattice with anionic dopants (C^{4-} and S^{2-}).[16,27]

Comparison of the Performance of car-ZnO NPs toward MB, MO, and Cr(VI) Removal. The evaluation of the photocatalytic performance of the synthesized photocatalyst involved assessing its ability to degrade MB, MO, and Cr(VI) under UV light exposure. The parameters examined in the photocatalytic degradation process included the concentration of pollutants, the pH of the pollutant solution, the dosage of the photocatalyst, and various types of synthesized ZnO NPs.

Effect of Pollutant Concentration. Experiments were conducted to investigate the behavior of the photocatalyst across various pollutant concentrations (3, 5, and 7 ppm) under UV light exposure. The absorbance of the samples was measured and recorded at various time intervals, and the results were subsequently compared with the initial absorption levels before the photocatalytic process. Figure 9 represents the obtained results and shows that the photocatalytic degradation of all pollutants increases as the initial concentration decreases. This observation was anticipated due to the inhibitive effect that pollutant adsorption imparts on the surface of the photocatalyst that leads to reduction in available adsorption sites and consequently diminishes degradation efficiency upon further photocatalytic treatment of the pollutants.[10,48] Similar results have also been reported by other researchers.[48−50] Based on the data presented in Figure 9, the highest rate of pollutant degradation was observed at a concentration of 3

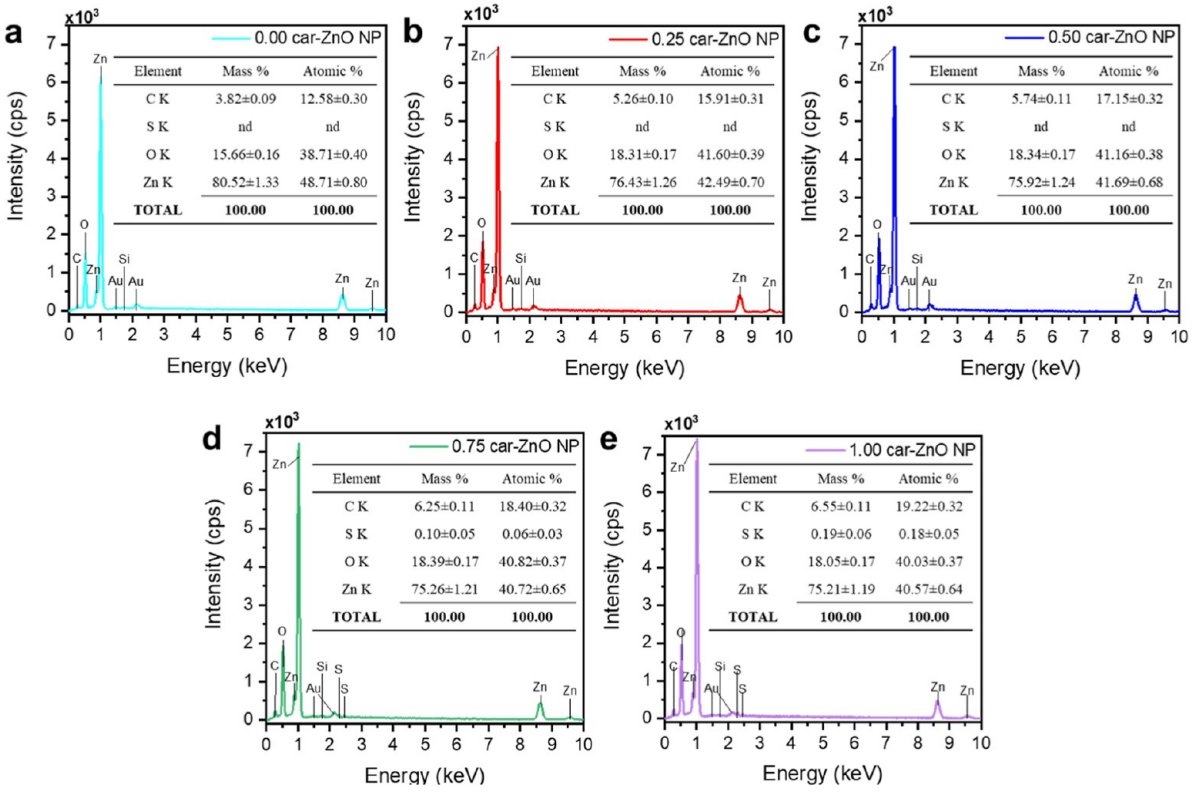

Figure 7. EDX spectrum of synthesized ZnO NPs, and insets are the corresponding quantitative measurements. (a) 0.00 car-ZnO, (b) 0.25 car-ZnO, (c) 0.50 car-ZnO, (d) 0.75 car-ZnO, and (e) 1.00 car-ZnO.

https://doi.org/10.1021/acsomega.4c06074
ACS Omega 2025, 10, 9919−9937

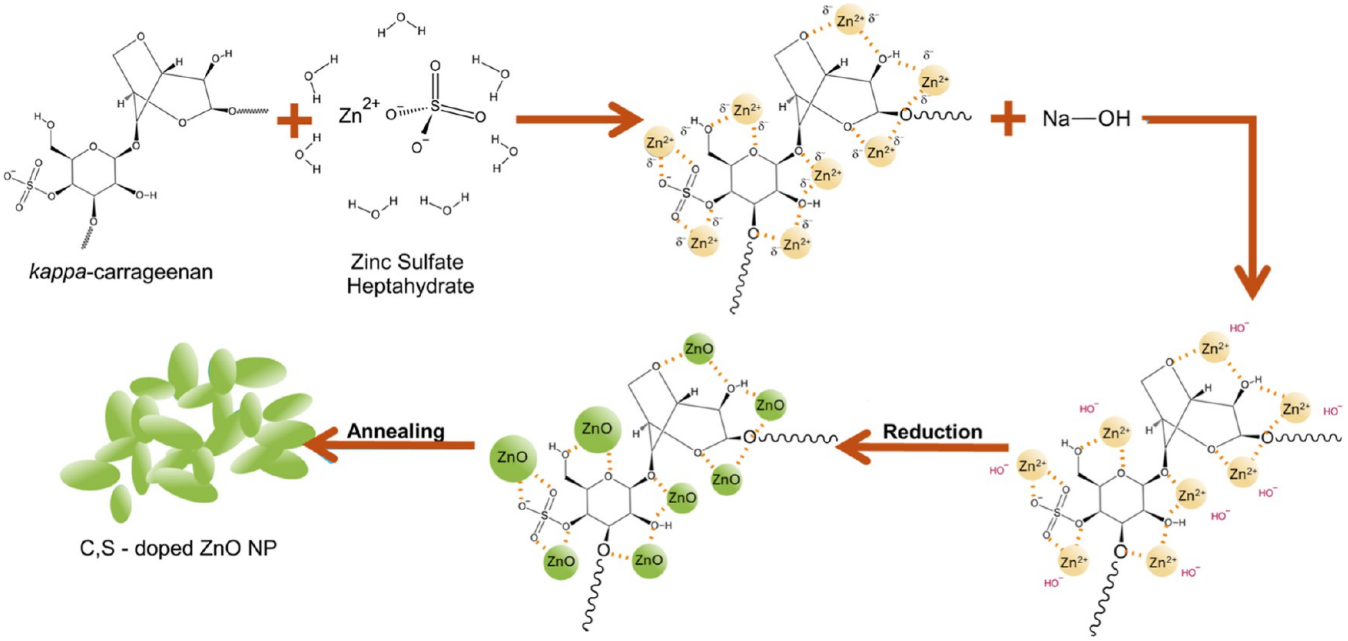

Figure 8. Proposed mechanism for the formation of car-ZnO NPs.

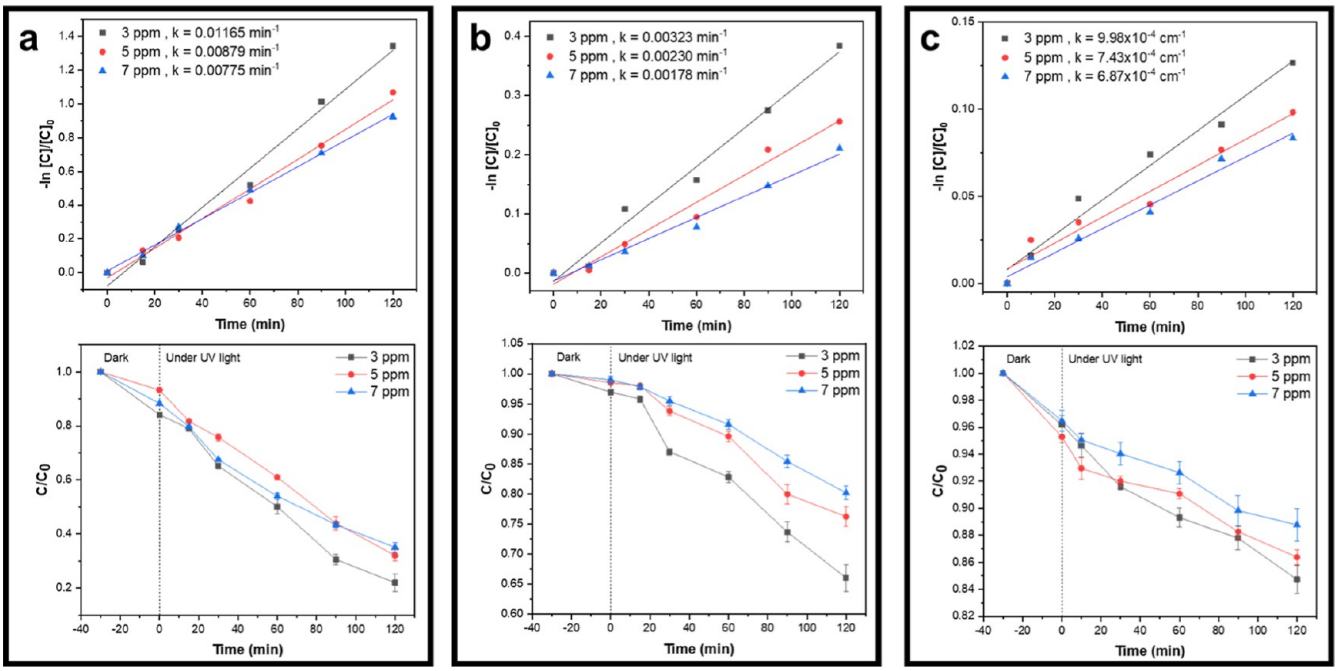

Figure 9. First-order kinetic plots of $\ln[C/C_0]$ and linear plot of C/C_0 vs time using 250 mg/L of 0.75 car-ZnO at normal solution pH and varying pollutant concentration: (a) methylene blue, (b) methyl orange, and (c) hexavalent chromium. Error bars represent the standard deviation of triplicate measurements for the linear plot of C/C_0 vs time.

ppm for all pollutants. Therefore, a 3 ppm concentration of dye/heavy metal was selected as the optimal concentration for further experiments.

Effect of ZnO Photocatalyst Dosage. The impact of photocatalyst concentration on the photocatalytic degradation of dye/heavy metal solutions was evaluated by employing a range of photocatalyst concentrations varying from 250 to 1500 mg L^{-1}. As illustrated in Figure 10a–c, the photocatalyst concentration has a direct relationship with photodegradation efficiency within the concentration range of 250 to 1000 mg L^{-1}, reflected as a striking increment in degradation efficiency, which peaks at 1000 mg L^{-1} after 120 min of irradiation. Beyond this point, the opposite relationship is noted, as the photodegradation efficiency of 1500 mg L^{-1} lagged behind that of 1000 mg L^{-1}. The increase in the degradation rate as the catalyst concentration rises is attributed to the expansion of active areas available for dye/heavy metal degradation. However, a continued increase in catalyst concentration would result in the accumulation of suspended nanoparticles, ultimately exceeding the transmission of light in the pollutant–catalyst suspension system. This results in a lowered rate of photoirradiation on the photocatalyst active sites despite their

https://doi.org/10.1021/acsomega.4c06074
ACS Omega 2025, 10, 9919–9937

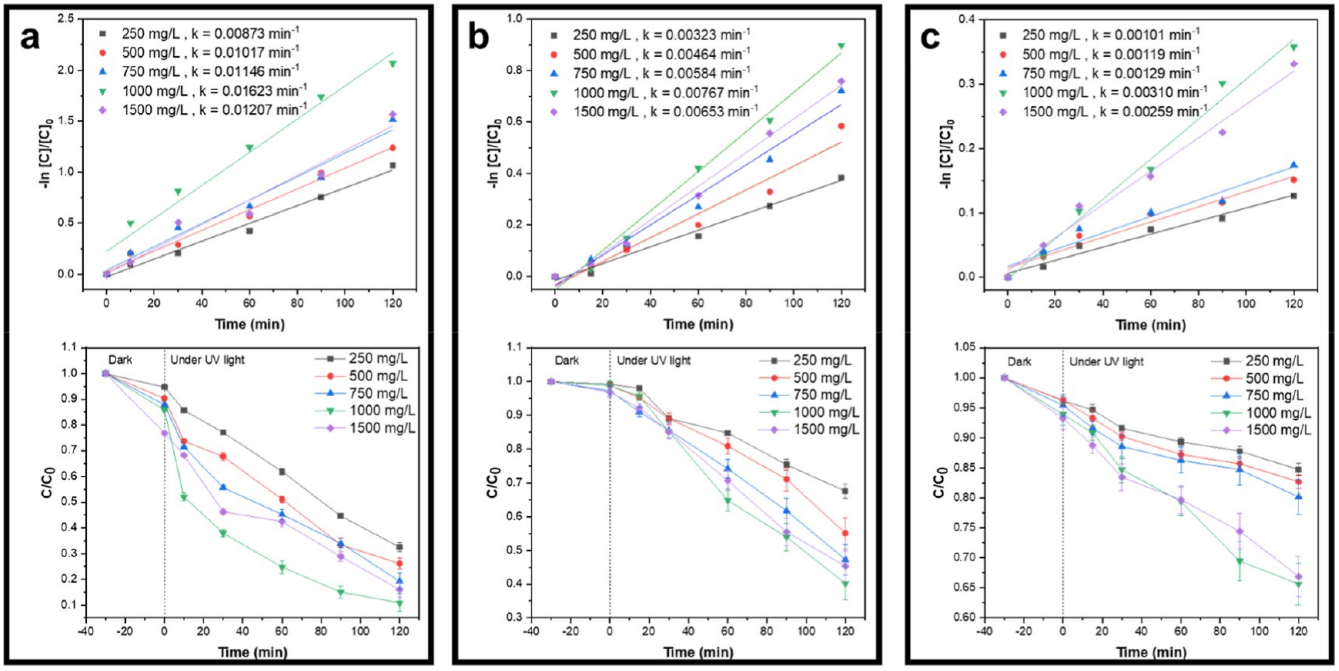

Figure 10. First-order kinetic plots of $\ln[C/C_0]$ and linear plot of C/C_0 vs time using varying photocatalyst dosage of 0.75 car-ZnO at normal solution pH and 3 ppm pollutant concentration: (a) methylene blue, (b) methyl orange, and (c) hexavalent chromium. Error bars represent the standard deviation of triplicate measurements for the linear plot of C/C_0 vs time.

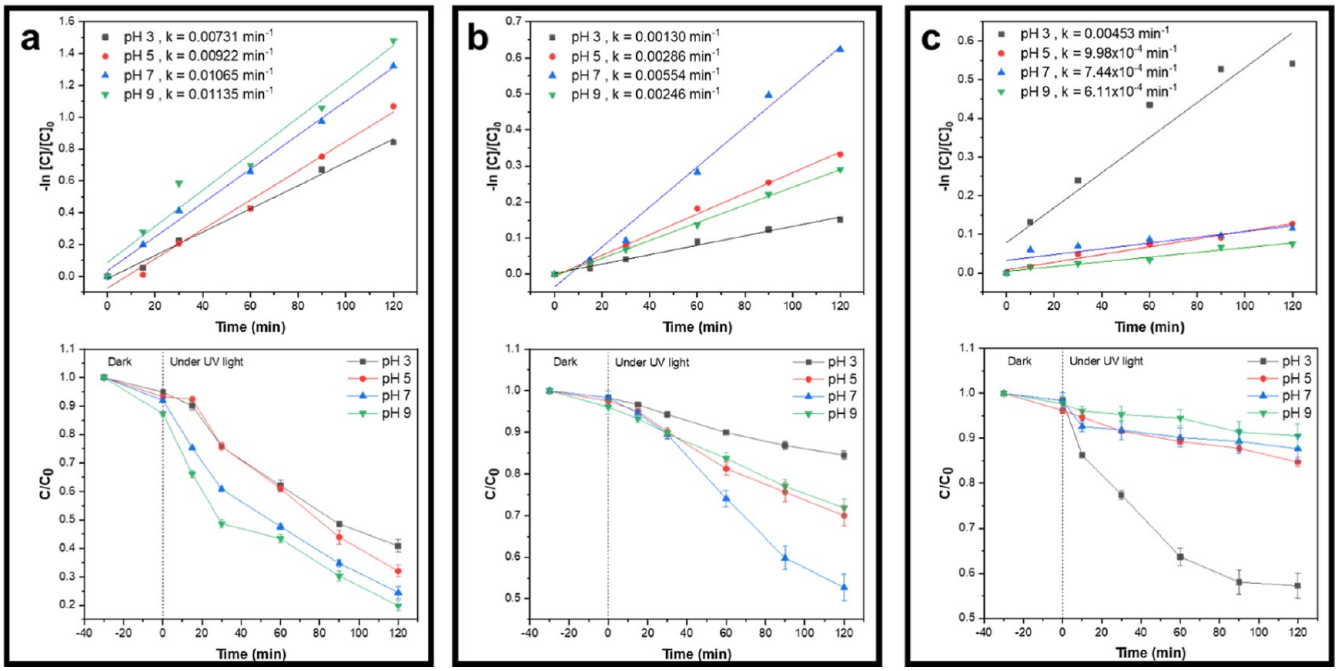

Figure 11. First-order kinetic plots of $\ln[C/C_0]$ and linear plot of C/C_0 vs time using 250 mg/L of 0.75 car-ZnO at varying pollutant solution pH and 3 ppm pollutant concentration: (a) methylene blue, (b) methyl orange, and (c) hexavalent chromium. Error bars represent the standard deviation of triplicate measurements for the linear plot of C/C_0 vs time.

increased number, hence the substantial efficiency reduction with 1500 mg L^{-1} concentration in Figure 10 across all pollutants. Other studies have also reported comparable observations.[10,51,52] Therefore, a concentration of 1000 mg L^{-1} was chosen as the optimal dosage of photocatalyst for the photocatalytic reaction under the experimental conditions.

Effect of Pollutant Solution pH. The amphoteric nature of most semiconductor oxides makes the pH of dispersions a significant factor in governing the rate of reactions occurring on the surface of semiconductor particles. This is because alterations in pH influence the surface-charge properties of the photocatalysts, potentially causing shifts in the redox potentials of their VB and conduction band (CB), which, in turn, affect the interfacial charge transfer processes. This factor is also of great importance as industrial effluents often deviate from the neutral pH, e.g., the pollutant solution pH used in this work

https://doi.org/10.1021/acsomega.4c06074
ACS Omega 2025, 10, 9919−9937

was recorded to be 7.1, 5.5, and 6.8 for MB, MO, and Cr(VI), respectively, prior to the photocatalytic reaction. Thus, there is a need to examine the effects of the pH to determine the optimal degradation conditions specifically suited to the nature of the pollutant.

The first-order kinetic profiles of pollutant degradation at various pollutant solution pH values are depicted in Figure 11. Figure 11a shows a favorable effect of increasing the MB solution pH on the extent of photocatalysis of MB. As the pH rose from 3 to 9, the degradation rate of the pollutant increased from 0.00731 min^{-1} to 0.01135 min^{-1}. The adverse effect of acidic pH conditions on the photocatalytic degradation rate may stem from heightened dye molecule adsorption at these pH levels, resulting in a pollutant covering the catalyst surface and subsequent reduction in UV radiation absorption. Conversely, the excess hydroxide ions (OH^-) at higher pH levels facilitate the photogeneration of hydroxyl radicals ($^{\bullet}OH$),[53,54] hence the distinct degradation rate improvement featured in Figure 11a. These findings can be further elucidated through the photocatalyst's point of zero charge (pH_{pzc}) determined to be at pH 8.61 (Figure 12). At

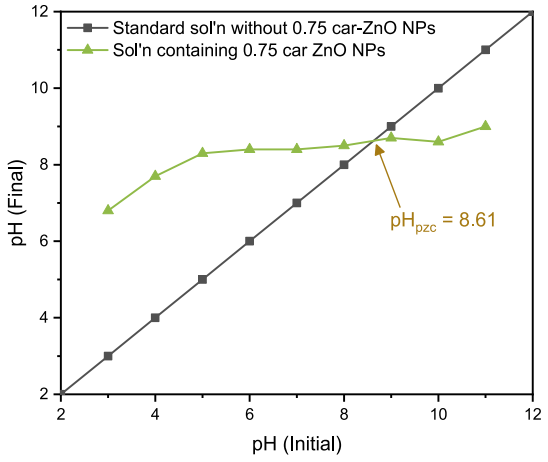

Figure 12. Point of zero charge (pH_{pzc}) of 0.75 car-ZnO NP, determined by the pH drift method.

pH levels higher than pH_{pzc}, the photocatalyst bears a negatively charged surface that enhances the degradation of the cationic dyes. Thus, these notions predicate the experimental results, with the highest MB photodegradation rate at pH 9.

In contrast with the cationic nature of MB, the anionic characteristic of the MO warrants the opposite charge on the surface of the ZnO photocatalyst for better degradation performance. To induce a positively charged ZnO surface for enhanced acidic pollutant adherence, the degradation process must be done at pH levels lower than its pH_{pzc}. Moreover, the reported pK_a of MO is 3.8 ± 0.02, indicating a shift toward its anionic (deprotonated) form at pH values greater than the pK_a.[55,56] This pH-dependent association is clearly depicted in Figure 11b, wherein pH conditions below the pK_a of the MO showed the lowest degradation performance. Concordantly, a relatively diminished performance was recorded above the pH_{pzc} of ZnO. This may be due to the decrease in $^{\bullet}OH$ oxidation potential at high pH levels due to the prevalence of anionic MO that competes with the OH^- groups, reducing their binding capacity to ZnO.[56] Inversely, the photodegradation performance was comparatively augmented at pH levels between the pK_a and pH_{pzc} range, with the most suitable pH condition for the degradation of MO recorded at pH 7 in agreement with the stipulated parameters.

The Cr(VI) pollutant exists predominantly as dichromate ($Cr_2O_7^{2-}$) species in acidic environments, whereas it exists as chromate (CrO_4^{2-}) or hydrogen chromate ($HCrO_4^-$) ions in alkaline environments. Thus, the reduction of Cr^{6+} to Cr^{3+} may proceed in any of the reactions below according to the solution pH[8]

$$Cr_2O_2^{-7} + 14H^+ + 6e^- \rightarrow 2Cr^{3+} + 7H_2O \text{ (acidic condition)}$$

$$CrO_2^{-4} + 8H^+ + 3e^- \rightarrow Cr^{3+} + 4H_2O \text{ (neutral condition)}$$

$$CrO_2^{-4} + 4H_2O + 3e^- \rightarrow Cr(OH)_3 + 5OH^- \text{ (alkaline condition)}$$

When subjected to photoirradiation, the pH of the chromate solution tends to decrease from nearly neutral (pH 6.8) to acidic. This signifies that the mechanism governing the reduction of Cr(VI) involved a shift from one route to another, as stated in the reactions described above. The correlation between the degradation rate and Cr(VI) solution pH is featured in Figure 11c. The plot shows the stark impact of pH on the extent of degradation with the best outcome attained at pH 3. This result conformed with the previous point on the induced charge on the photocatalyst's surface, wherein a positively charged ZnO surface (protonated) is needed to electrostatically adsorb the negatively charged $HCrO_4^-$ ions for the photoconversion process to proceed via electron transfer.

Effect of Different car-ZnO NPs. In order to determine the effects of the different ZnO NPs synthesized with varying carrageenan extract concentrations on the photodegradation rate of dyes/heavy metal solutions, the same photoirradiation investigations were conducted but using the optimal parameters from previous experiments—the same pollutant concentration of 3 ppm, photocatalyst loading of 1000 mg/L, and solution pH of 9, 7, and 3 for MB, MO, and Cr(VI), respectively.

The findings depicted in Figure 13 demonstrate an overall improvement in the photodegradation efficiency of carrageenan-mediated ZnO NPs compared to unmodified ZnO NPs for all pollutants. Additionally, it was apparent that the efficiency increased with increasing carrageenan content, peaking at 0.75 wt % concentration. It is also worth noting that the photocatalytic degradation in descending order—0.75 car-ZnO > 1.00 car-ZnO > 0.50 car-ZnO > 0.25 car-ZnO > 0.00 car-ZnO—conformed with the order of increasing crystallite size band gap energy in Table 1. These findings further exemplify the expected photodegradation efficiency improvement brought by the narrowed band gap due to C−S doping that simultaneously enhanced the migration of charge carriers and inhibited the recombination of the photogenerated electron−hole charge carriers. Figure 14 shows the dark adsorption and photodegradation of 0.75 car-ZnO NPS which elucidates the total pollutant degradation. Furthermore, the photodegradation performance of car-ZnO NP is on par with or marginally superior to that of other ZnO-based photocatalysts reported in the literature (Table 3).

https://doi.org/10.1021/acsomega.4c06074
ACS Omega 2025, 10, 9919−9937

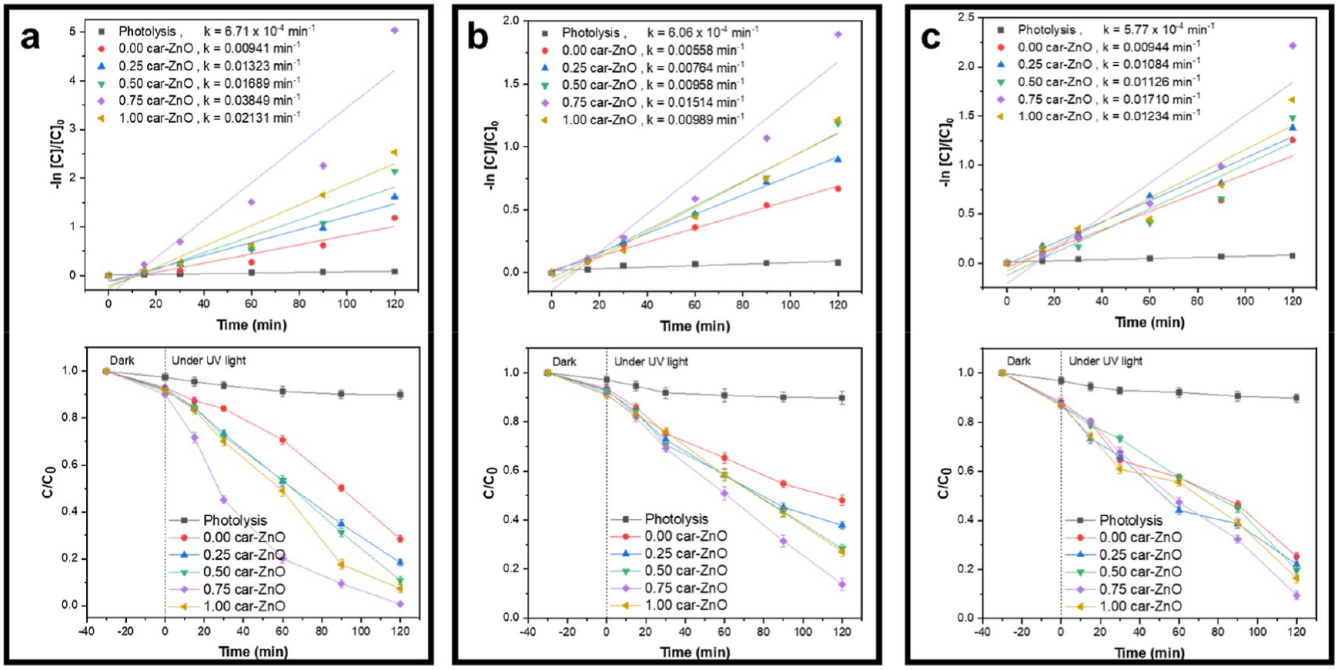

Figure 13. First-order kinetic plots of $\ln[C/C_0]$ and linear plot of C/C_0 vs time using 1000 mg/L of different car-ZnO NPs at pollutant solution pH (pH 9, 7, and 3 for MB, MO, and Cr(VI), respectively) and 3 ppm pollutant concentration: (a) methylene blue, (b) methyl orange, and (c) hexavalent chromium. Error bars represent the standard deviation of triplicate measurements for the linear plot of C/C_0 vs time.

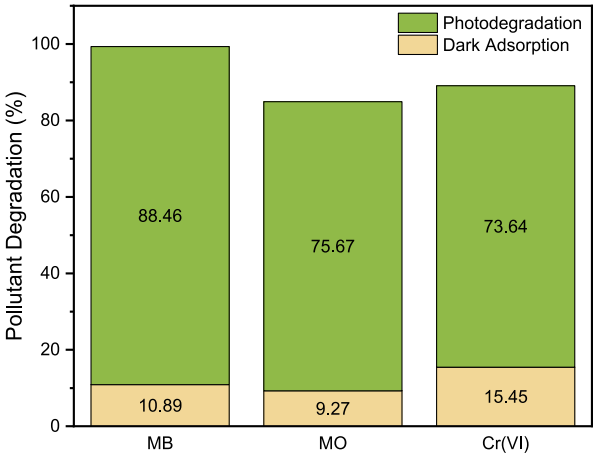

Figure 14. Percent degradation of MB, MO, and Cr(VI) using 1000 mg/L of 0.75 car-ZnO NPs at pollutant solution pH (pH 9, 7, and 3 for MB, MO, and Cr(VI), respectively) and 3 ppm pollutant concentration.

In addition, a recyclability test is conducted to validate the catalyst's photostability during repetitive photodegradation. Figure 15 shows a minimal loss of around 6.24%, 8.00%, and 8.74% of the initial photocatalytic performance of car-ZnO NP for the degradation of MB, MO, and Cr(VI), respectively, after five (5) cycles. This data proves that the synthesized car-ZnO NPs have high photostability over various reaction cycles.

Photocatalytic Process Mechanism. The incorporation of nonmetal dopants plays a crucial role in improving the photocatalytic degradation activity of ZnO by altering its band structure. In the photocatalytic mechanism of ZnO shown in Figure 16, exposure to UV light leads to the excitation of ZnO's valence electrons, prompting their transition from the VB to CB, producing electron−hole pairs. In effect, positive holes (h^+) are formed within the VB, which, coupled with the free electron, participate in the surface reactions of the photocatalyst in conjunction with the adsorbed water molecules that form superoxide ions ($^{\bullet}O^{2-}$) and hydroxyl radicals ($^{\bullet}OH$), facilitating the degradation of pollutants (MB, MO, and Cr^{6+}).[8,10,59]

Table 3. Performance of car-ZnO NPs as a Photocatalyst in Pollutant Degradation in Comparison with Unmodified ZnO-Based Photocatalysts

photocatalyst type	preparation method	pollutant	reaction time (min)	degradation (%)	literature
ZnO	green synthesized	MB	90	88.73	10
ZnO	green synthesized	MB	105	98	57
ZnO	sol−gel	MO	180	76.31	49
ZnO	sol−gel	MO	240	80	58
ZnO	green synthesized	Cr(VI)	90	75	3
ZnO	solvothermal	Cr(VI)	300	70	8
C,S-doped ZnO	green synthesized	MB	120	99.35	in this study
C,S-doped ZnO	green synthesized	MO	120	84.94	in this study
C,S-doped ZnO	green synthesized	Cr(VI)	120	89.09	in this study

https://doi.org/10.1021/acsomega.4c06074
ACS Omega 2025, 10, 9919−9937

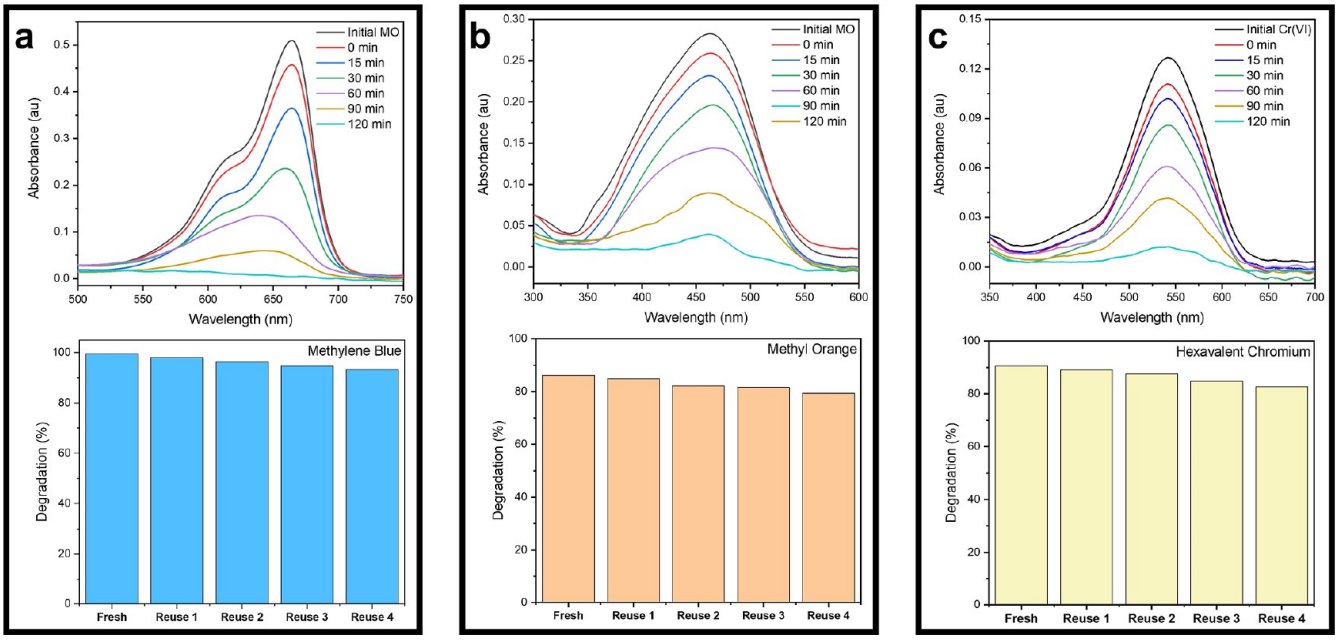

Figure 15. Photocatalytic activity and reusability study of 0.75 car-ZnO NPs was evaluated toward the photodegradation of (a) methylene blue, (b) methyl orange, and (c) hexavalent chromium.

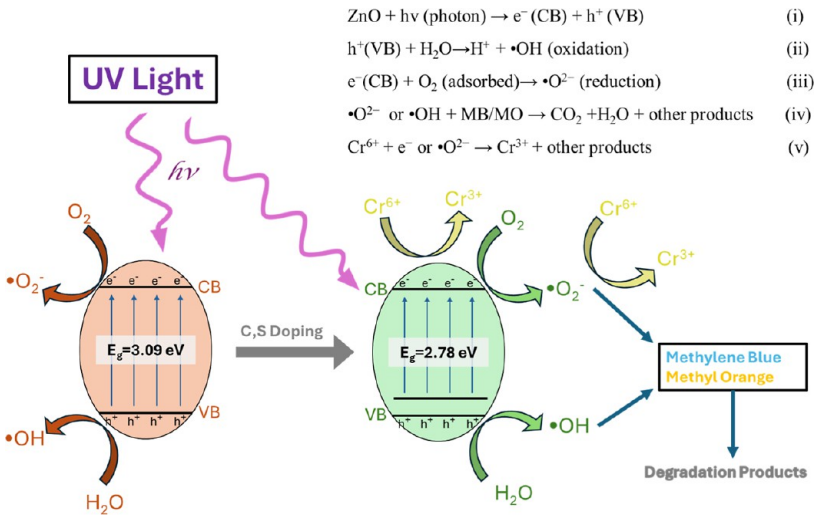

Figure 16. Proposed mechanism of the photocatalytic process.

For MB and MO, the degradation primarily involves the breakdown of aromatic rings and chromophores, leading to smaller organic compounds, such as sulfonic acid derivatives, carbon dioxide, and other intermediates.[60,61] In contrast, the primary product of the reduction of CR(VI) is Cr(III), which precipitates as $Cr(OH)_3$ under alkaline conditions or remains as Cr(III) ions in solution. Unlike organic pollutants, Cr(VI) reduction does not produce complex organic intermediates, but the conversion to Cr(III) significantly reduces the toxicity and environmental impact.

Nonmetal doping was implemented to expand the light absorption range of ZnO, utilizing carbon and sulfur derived from kappa-carrageenan to substitute oxygen in the ZnO lattice. The result of this modification is the formation of a localized state above the VB of ZnO (Figure 16) that effectively reduces the band gap. Therefore, the reduced band gap allows ZnO to capture a wider range of light wavelengths, thereby improving the efficiency of UV light utilization. Additionally, the altered band structure induced by the nonmetallic dopants above the VB serves as traps for holes, aiding in the effective separation of photoexcited electron−hole pairs. This hole-trapping mechanism is essential for preventing recombination and minimizing the loss of photo-induced charge carriers before their participation in photo-degradation reactions.[12,13,16]

The prolonged duration of these photoinduced charge carriers increases the abundance of electrons and holes for redox reactions including the formation of hydroxyl radicals (•OH) from water molecules. The substantial increase in the rate of pollutant photodegradation stems from the synergistic impact of a reduced band gap, effective charge separation, and enhanced light absorption facilitated by the inclusion of nonmetallic (C and S) dopants.[12,13] This superior performance is evidenced by the enhanced photodegradation of model contaminants, such as MB, MO, and Cr(VI).

https://doi.org/10.1021/acsomega.4c06074
ACS Omega 2025, 10, 9919−9937

CONCLUSIONS

The present study demonstrates the successful synthesis of carrageenan-modified zinc oxide nanoparticles (car-ZnO NPs) with enhanced photocatalytic properties for pollutant degradation. The use of κ-carrageenan in the synthesis led to notable modifications in the car-ZnO NPs, including reduced band gaps and smaller crystallite sizes, as confirmed by XRD analysis. UV−visible spectroscopic analysis further indicated a decreased band gap energy in car-ZnO NPs compared with unmodified ZnO NPs, attributed to the incorporation of residual carbon and sulfur from κ-carrageenan. SEM and TEM revealed that car-ZnO NPs synthesized with 0.75% (w/v) κ-carrageenan exhibited the most uniformly distributed particle sizes. The 0.75 car-ZnO NP catalyst demonstrated superior photocatalytic efficiency, achieving enhanced removal efficiencies of methylene blue (99.35%), methyl orange (84.94%), and hexavalent chromium (Cr(VI)) (89.09%) within 120 min of irradiation, outperforming unmodified ZnO NPs by 1.43, 1.74, and 1.25 times, respectively. This improvement is attributed to the reduced band gap and carbon and sulfur doping, which enhanced the charge carrier dynamics. car-ZnO NPs also showed excellent photostability and recyclability, highlighting their potential for eco-friendly water treatment applications. Future work should focus on investigating broader applications, conducting in-depth mechanistic studies, and scaling up for large-scale water treatment, which are recommended. Advancing green synthesis methods while assessing the long-term environmental impact will be essential for sustainable development in this field.

ASSOCIATED CONTENT

Data Availability Statement

The data supporting this study are provided throughout the manuscript. Raw data are not publicly available due to ongoing intellectual property considerations but may be obtained from the corresponding author upon reasonable request, subject to confidentiality agreements.

AUTHOR INFORMATION

Corresponding Author

Arnold A. Lubguban − *Center for Sustainable Polymers, Mindanao State University—Iligan Institute of Technology, Iligan City 9200, Philippines; Department of Chemical Engineering and Technology, Mindanao State University—Iligan Institute of Technology, Iligan City 9200, Philippines;* orcid.org/0000-0001-6077-8234; Phone: +63-9396420752; Email: arnold.lubguban@g.msuiit.edu.ph

Authors

Dan Michael A. Asequia − *Center for Sustainable Polymers, Mindanao State University—Iligan Institute of Technology, Iligan City 9200, Philippines;* orcid.org/0009-0003-4628-3229

Daisy Jane D. Erjeno − *Center for Sustainable Polymers, Mindanao State University—Iligan Institute of Technology, Iligan City 9200, Philippines*

Carlo Kurt F. Osorio − *Center for Sustainable Polymers, Mindanao State University—Iligan Institute of Technology, Iligan City 9200, Philippines;* orcid.org/0009-0002-1390-6752

Christine Joy M. Omisol − *Center for Sustainable Polymers, Mindanao State University—Iligan Institute of Technology, Iligan City 9200, Philippines;* orcid.org/0000-0002-9405-0070

Renzo Miguel Hisona − *Center for Sustainable Polymers, Mindanao State University—Iligan Institute of Technology, Iligan City 9200, Philippines*

Blessy Joy M. Aguinid − *Center for Sustainable Polymers, Mindanao State University—Iligan Institute of Technology, Iligan City 9200, Philippines*

Sitti Zayda B. Halun − *Seaweed Research and Development Center and Institute of Oceanography and Environmental Science, Mindanao State University—Tawi-Tawi, Tawi-Tawi 7500, Philippines*

Joshua B. Zoleta − *Department of Materials Resources Engineering and Technology, Mindanao State University—Iligan Institute of Technology, Iligan City 9200, Philippines*

Roberto M. Malaluan − *Center for Sustainable Polymers, Mindanao State University—Iligan Institute of Technology, Iligan City 9200, Philippines; Department of Chemical Engineering and Technology, Mindanao State University—Iligan Institute of Technology, Iligan City 9200, Philippines*

Arnold C. Alguno − *Center for Sustainable Polymers, Mindanao State University—Iligan Institute of Technology, Iligan City 9200, Philippines; Department of Physics, Mindanao State University—Iligan Institute of Technology, Iligan City 9200, Philippines*

Complete contact information is available at: https://pubs.acs.org/10.1021/acsomega.4c06074

Author Contributions

The manuscript was written through the contributions of all authors. All authors have given approval to the final version of the manuscript.

Notes

The authors declare no competing financial interest.

ACKNOWLEDGMENTS

The work was supported by the Republic of the Philippines—Department of Science and Technology's financial grant through the NICER—R&D Center for Sustainable Polymers.

ABBREVIATIONS

NP, nanoparticle; car-ZnO NPs, carrageenan-mediated ZnO nanoparticles; MB, methylene blue; MO, methyl orange; Cr(VI), hexavalent chromium.

REFERENCES

(1) Gharbani, P.; Mehrizad, A.; Mosavi, S. A. Optimization, Kinetics and Thermodynamics Studies for Photocatalytic Degradation of Methylene Blue Using Cadmium Selenide Nanoparticles. *Npj Clean Water* **2022**, *5* (1), 34.

(2) Zahid, Z.; Rauf, A.; Javed, M.; Alhujaily, A.; Iqbal, S.; Amjad, A.; Arif, M.; Hussain, S.; Bahadur, A.; Awwad, N. S.; Ibrahium, H. A.; Al-Fawzan, F. F.; Elkaeed, E. B. Photocatalytic Reduction of Cr(VI) to Cr(III) and Photocatalytic Degradation of Methylene Blue and Antifungal Activity of Ag/TiO2 Composites Synthesized via the Template Induced Route. *Inorganics* **2023**, *11* (3), 133.

(3) Onwudiwe, D. C.; Oyewo, O. A.; Ogunjinmi, O. E.; Ojelere, O. Hexavalent Chromium Reduction by ZnO, SnO2 and ZnO-SnO2 Synthesized Using Biosurfactants from Extract of Solanum Macrocarpon. *South Afr. J. Chem. Eng.* **2021**, *38*, 21−33.

(4) United Nations. *Partnerships and Cooperation for Water*; United Nations Educational, Scientific and Cultural Organization: Paris, France, 2023.

https://doi.org/10.1021/acsomega.4c06074
ACS Omega 2025, 10, 9919−9937

(5) Vaiano, V.; De Marco, I. Removal of Azo Dyes from Wastewater through Heterogeneous Photocatalysis and Supercritical Water Oxidation. *Separations* **2023**, *10* (4), 230.
(6) Malekkiani, M.; Heshmati Jannat Magham, A.; Ravari, F.; Dadmehr, M. Facile Fabrication of Ternary MWCNTs/ZnO/Chitosan Nanocomposite for Enhanced Photocatalytic Degradation of Methylene Blue and Antibacterial Activity. *Sci. Rep.* **2022**, *12* (1), 5927.
(7) Zafar, S.; Bukhari, D. A.; Rehman, A. Azo Dyes Degradation by Microorganisms − An Efficient and Sustainable Approach. *Saudi J. Biol. Sci.* **2022**, *29* (12), 103437.
(8) Kangralkar, M. V.; Manjanna, J.; Momin, N.; Rane, K. S.; Nayaka, G. P.; Kangralkar, V. A. Photocatalytic Degradation of Hexavalent Chromium and Different Staining Dyes by ZnO in Aqueous Medium under UV Light. *Environ. Nanotechnol. Monit. Manage.* **2021**, *16*, 100508.
(9) Asoubar, S.; Mehrizad, A.; Behnajady, M. A.; Ramazani, M. E.; Gharbani, P. Hexavalent Chromium Reduction and Rhodamine B Degradation by Visible-Light-Driven Photocatalyst of Stannum Indium Sulfide-Samarium Vanadate. *Npj Clean Water* **2023**, *6* (1), 27.
(10) Alshehri, A. A.; Malik, M. A. Biogenic Fabrication of ZnO Nanoparticles Using Trigonella Foenum-Graecum (Fenugreek) for Proficient Photocatalytic Degradation of Methylene Blue under UV Irradiation. *J. Mater. Sci. Mater. Electron.* **2019**, *30* (17), 16156−16173.
(11) Venkatesan, S.; Suresh, S.; Ramu, P.; Arumugam, J.; Thambidurai, S.; Pugazhenthiran, N. Methylene Blue Dye Degradation Potential of Zinc Oxide Nanoparticles Bioreduced Using Solanum Trilobatum Leaf Extract. *Results Chem.* **2022**, *4*, 100637.
(12) Hosny, N. M.; Gomaa, I.; Elmahgary, M. G.; Ibrahim, M. A. ZnO Doped C: Facile Synthesis, Characterization and Photocatalytic Degradation of Dyes. *Sci. Rep.* **2023**, *13* (1), 14173.
(13) Kumari, V.; Mittal, A.; Jindal, J.; Yadav, S.; Kumar, N. S.-. S-N- and C-doped ZnO as semiconductor photocatalysts: A review. *Front. Mater. Sci.* **2019**, *13* (1), 1−22.
(14) Patil, P.; Sannakki, B.; Mathad, S.; Veena, E.; Gandad, S. A Review on Non-Metal and Metal Doped ZnO: Fundamental Properties and Applications. *Acta Period. Technol.* **2023**, No. 54, 277−299.
(15) Zhang, X.; Qin, J.; Hao, R.; Wang, L.; Shen, X.; Yu, R.; Limpanart, S.; Ma, M.; Liu, R. Carbon-Doped ZnO Nanostructures: Facile Synthesis and Visible Light Photocatalytic Applications. *J. Phys. Chem. C* **2015**, *119* (35), 20544−20554.
(16) Mirzaeifard, Z.; Shariatinia, Z.; Jourshabani, M.; Rezaei Darvishi, S. M. ZnO Photocatalyst Revisited: Effective Photocatalytic Degradation of Emerging Contaminants Using S-Doped ZnO Nanoparticles under Visible Light Radiation. *Ind. Eng. Chem. Res.* **2020**, *59* (36), 15894−15911.
(17) Xie, X.-Y.; Zhan, P.; Li, L.-Y.; Zhou, D.-J.; Guo, D.-Y.; Meng, J.-X.; Bai, Y.; Zheng, W.-J. Synthesis of S-Doped ZnO by the Interaction of Sulfur with Zinc Salt in PEG200. *J. Alloys Compd.* **2015**, *644*, 383−389.
(18) Erjeno, D. J. D.; Asequia, D. M. A.; Osorio, C. K. F.; Omisol, C. J. M.; Etom, A. E.; Hisona, R. M. R.; Tilendo, A. C.; Triana, A. P. G.; Dumancas, G. G.; Zoleta, J. B.; Alguno, A. C.; Malaluan, R. M.; Lubguban, A. A. Facile Synthesis of Band Gap-Tunable Kappa-Carrageenan-Mediated C,S-Doped TiO_2 Nanoparticles for Enhanced Dye Degradation. *ACS Omega* **2024**, *9* (19), 21245−21259.
(19) Khalyavka, T.; Bondarenko, M.; Shcherban, N.; Petrik, I.; Melnyk, A. Effect of the C and S Additives on Structural, Optical, and Photocatalytic Properties of TiO2. *Appl. Nanosci.* **2019**, *9* (5), 695−702.
(20) Lei, C.; Chen, M.; Zhong, N.; Yao, W.; Xiong, Y.; Zhang, X.; Lu, C. C/S-TiO2 Nanospheres with Enhanced Visible-Light Response for Formaldehyde Degradation of Particleboard. *IOP Conf. Ser. Earth Environ. Sci.* **2022**, *983* (1), 012108.
(21) Ali Ansari, S.; Parveen, N.; Aljaafari, A.; Alshoaibi, A.; Alsulaim, G. M.; Waqas Alam, M.; Zahid Ansari, M. Novel Furfural-Complexed Approach to Synthesizing Carbon-Doped ZnO with Breakthrough Photocatalytic Efficacy. *J. Adv. Res.* **2024**, S2090-123224003576.
(22) Chang, Q.-Q.; Cui, Y.-W.; Zhang, H.-H.; Chang, F.; Zhu, B.-H.; Yu, S.-Y. C-Doped ZnO Decorated with Au Nanoparticles Constructed from the Metal−Organic Framework ZIF-8 for Photodegradation of Organic Dyes. *RSC Adv.* **2019**, *9* (22), 12689−12695.
(23) Zhang, L.; Zhu, X.; Wang, Z.; Yun, S.; Guo, T.; Zhang, J.; Hu, T.; Jiang, J.; Chen, J. Synthesis of ZnO Doped High Valence S Element and Study of Photogenerated Charges Properties. *RSC Adv.* **2019**, *9* (8), 4422−4427.
(24) Rini, A. S.; Dewi, R.; Asriani, R.; Rati, Y. Biosynthesis of Sulfur-Doped Zinc Oxide Using Bidara Leaf Extract. *J. Phys. Conf. Ser.* **2023**, *2596* (1), 012011.
(25) Villanueva, R. D.; Romero, J. B.; Montaño, M. N. E.; De La Peña, P. O. Harvest Optimization of Four Kappaphycus Species from the Philippines. *Biomass Bioenergy* **2011**, *35* (3), 1311−1316.
(26) Wiryawan, A.; Retnowati, R.; Burhan, P.; Syekhfani, S. METHOD OF ANALYSIS FOR DETERMINATION OF THE CHROMIUM (Cr) SPECIES IN WATER SAMPLES BY SPECTROPHOTOMETRY WITH DIPHENYLCARBAZIDE. *J. Environmental Eng. Sustain. Technol.* **2018**, *5* (1), 37.
(27) Cho, S.; Jang, J.-W.; Lee, J. S.; Lee, K.-H. Carbon-Doped ZnO Nanostructures Synthesized Using Vitamin C for Visible Light Photocatalysis. *CrystEngComm* **2010**, *12* (11), 3929.
(28) Bouasla, N.; Abderrahmane, S.; Athmani, S.; Oulabbas, A.; Bououdina, M. ZnO Nanoparticles and Biocidal Effect of Nanostructured ZnO Films on Escherichia Coli. *Desalination Water Treat* **2018**, *104*, 217−224.
(29) Guo, K. W. Property of Zinc Oxide (ZnO) Nanostructures Potential for Biomedical System and Its Common Growth Mechanism. *J. Appl. Biotechnol. Bioeng.* **2017**, *2* (5), 197−202.
(30) Manabeng, M.; Mwankemwa, B. S.; Ocaya, R. O.; Motaung, T. E.; Malevu, T. D. A Review of the Impact of Zinc Oxide Nanostructure Morphology on Perovskite Solar Cell Performance. *Processes* **2022**, *10* (9), 1803.
(31) Aldalbahi, A.; Alterary, S.; Ali Abdullrahman Almoghim, R.; Awad, M. A.; Aldosari, N. S.; Fahad Alghannam, S.; Nasser Alabdan, A.; Alharbi, S.; Ali Mohammed Alateeq, B.; Abdulrahman Al Mohsen, A.; Alkathiri, M. A.; Abdulrahman Alrashed, R. Greener Synthesis of Zinc Oxide Nanoparticles: Characterization and Multifaceted Applications. *Molecules* **2020**, *25* (18), 4198.
(32) Tu, N.; Nguyen, K. T.; Trung, D. Q.; Tuan, N. T.; Do, V. N.; Huy, P. T. Effects of Carbon on Optical Properties of ZnO Powder. *J. Lumin.* **2016**, *174*, 6−10.
(33) Osman, H.; Su, Z.; Ma, X.; Liu, S.; Liu, X.; Abduwayit, D. Synthesis of ZnO/C Nanocomposites with Enhanced Visible Light Photocatalytic Activity. *Ceram. Int.* **2016**, *42* (8), 10237−10241.
(34) Beltrán, J. J.; Barrero, C. A.; Punnoose, A. Relationship between Ferromagnetism and Formation of Complex Carbon Bonds in Carbon Doped ZnO Powders. *Phys. Chem. Chem. Phys.* **2019**, *21* (17), 8808−8819.
(35) Chandrasekar, P.; Vishista, K. Photocatalytic Activity of High Energy Ball Mill Derived (ZnO)1−x(C)x Nanocomposite. *Trans. Indian Inst. Met.* **2018**, *71* (8), 2051−2055.
(36) Tayyebi, A.; Soltani, T.; Lee, B.-K.; Outokesh, M.; Tayebi, M. Novel Visible Light Photocatalytic and Photoelectrochemical (PEC) Activity of Carbon-Doped Zinc Oxide/Reduced Graphene Oxide: Supercritical Methanol Synthesis with Enhanced Photocorrosion Suppression. *J. Alloys Compd.* **2017**, *723*, 1001−1010.
(37) Devi, L. G.; Kavitha, R. Enhanced Photocatalytic Activity of Sulfur Doped TiO2 for the Decomposition of Phenol: A New Insight into the Bulk and Surface Modification. *Mater. Chem. Phys.* **2014**, *143* (3), 1300−1308.
(38) Nakamoto, K. Infrared and Raman Spectra of Inorganic and Coordination Compounds. In *Handbook of Vibrational Spectroscopy*; John Wiley & Sons, Ltd, 2008..
(39) Elsupikhe, R. F.; Shameli, K.; Ahmad, M. B. Sonochemical Method for the Synthesis of Silver Nanoparticles in κ-Carrageenan

https://doi.org/10.1021/acsomega.4c06074
ACS Omega 2025, 10, 9919−9937

from Silver Salt at Different Concentrations. *Res. Chem. Intermed.* **2015**, *41* (11), 8515−8525.
(40) Agili, F. A.; Mohamed, S. F. Synthesis and Characterization of a Self-Crosslinked Organic Copolymer Kappa-Carrageenan/Polyacrylamide/Cetrimide (κ-CAR/PAAm/CI) Hydrogel with Antimicrobial and Anti-Inflammatory Activities for Wound Healing. *Chemistry* **2023**, *5* (4), 2273−2287.
(41) Dhewang, I. B.; Yudiati, E.; Subagiyo, S.; Alghazeer, R. Carrageenan Extraction of Kappaphycus Alvarezii Seaweed from Nusa Lembongan Waters Using Different Alkaline Treatments. *J. Kelaut. Trop.* **2023**, *26* (2), 238−244.
(42) Qu, G.; Fan, G.; Zhou, M.; Rong, X.; Li, T.; Zhang, R.; Sun, J.; Chen, D. Graphene-Modified ZnO Nanostructures for Low-Temperature NO_2 Sensing. *ACS Omega* **2019**, *4* (2), 4221−4232.
(43) Abliz, A.; Xue, X.; Liu, X.; Li, G.; Tang, L. Rational Design of Hydrogen and Nitrogen Co-Doped ZnO for High Performance Thin-Film Transistors. *Appl. Phys. Lett.* **2021**, *118* (12), 123504.
(44) Joshi, N.; Da Silva, L. F.; Shimizu, F. M.; Mastelaro, V. R.; M'Peko, J.-C.; Lin, L.; Oliveira, O. N. UV-Assisted Chemiresistors Made with Gold-Modified ZnO Nanorods to Detect Ozone Gas at Room Temperature. *Microchim. Acta* **2019**, *186* (7), 418.
(45) Mishra, D. K.; Mohapatra, J.; Sharma, M. K.; Chattarjee, R.; Singh, S. K.; Varma, S.; Behera, S. N.; Nayak, S. K.; Entel, P. Carbon Doped ZnO: Synthesis, Characterization and Interpretation. *J. Magn. Magn. Mater.* **2013**, *329*, 146−152.
(46) Jia, Y.; Wu, C.; Lee, B. W.; Liu, C.; Kang, S.; Lee, T.; Park, Y. C.; Yoo, R.; Lee, W. Magnetically Separable Sulfur-Doped $SnFe_2O_4$/Graphene Nanohybrids for Effective Photocatalytic Purification of Wastewater under Visible Light. *J. Hazard. Mater.* **2017**, *338*, 447−457.
(47) Cato, E.; Rossi, A.; Scherrer, N. C.; Ferreira, E. S. B. An XPS Study into Sulphur Speciation in Blue and Green Ultramarine. *J. Cult. Herit.* **2018**, *29*, 30−35.
(48) Anju Chanu, L.; Joychandra Singh, W.; Jugeshwar Singh, K.; Nomita Devi, K. Effect of Operational Parameters on the Photocatalytic Degradation of Methylene Blue Dye Solution Using Manganese Doped ZnO Nanoparticles. *Results Phys.* **2019**, *12*, 1230−1237.
(49) Al-Mamun, Md. R.; Iqbal Rokon, Md. Z.; Rahim, Md. A.; Hossain, Md. I.; Islam, Md. S.; Ali, Md. R.; Bacchu, M. S.; Waizumi, H.; Komeda, T.; Hossain Khan, M. Z. Enhanced Photocatalytic Activity of Cu and Ni-Doped ZnO Nanostructures: A Comparative Study of Methyl Orange Dye Degradation in Aqueous Solution. *Heliyon* **2023**, *9* (6), No. e16506.
(50) Ashar, A.; Bhatti, I. A.; Mohsin, M.; Yousaf, M.; Aziz, H.; Gul, A.; Hussain, T.; Bhutta, Z. A. Enhanced Solar Photocatalytic Activity of Thermally Stable I:ZnO/Glass Beads for Reduction of Cr(VI) in Tannery Effluent. *Front. Chem.* **2022**, *10*, 805913.
(51) Gerawork, M. Photodegradation of Methyl Orange Dye by Using Zinc Oxide − Copper Oxide Nanocomposite. *Optik* **2020**, *216*, 164864.
(52) Chakraborty, T.; Chakraborty, A.; Shukla, M.; Chattopadhyay, T. ZnO−Bentonite Nanocomposite: An Efficient Catalyst for Discharge of Dyes, Phenol and Cr(VI) from Water. *J. Coord. Chem.* **2019**, *72* (1), 53−68.
(53) Peng, G.; Chou, N.-N.; Lin, Y.-S.; Yang, C.-F.; Meen, T.-H. Comparison of the Degradation Effect of Methylene Blue for ZnO Nanorods Synthesized on Silicon and Indium Tin Oxide Substrates. *Materials* **2023**, *16* (12), 4275.
(54) Isai, K. A.; Shrivastava, V. S. Photocatalytic Degradation of Methylene Blue Using ZnO and 2%Fe−ZnO Semiconductor Nanomaterials Synthesized by Sol−Gel Method: A Comparative Study. *SN Appl. Sci.* **2019**, *1* (10), 1247.
(55) Saleh, S. M. ZnO Nanospheres Based Simple Hydrothermal Route for Photocatalytic Degradation of Azo Dye. *Spectrochim. Acta, Part A* **2019**, *211*, 141−147.
(56) Ibrahim, A. J. ZnO Nanostructure Synthesis for the Photocatalytic Degradation of Azo Dye Methyl Orange from Aqueous Solutions Utilizing Activated Carbon. *Anal. Methods Environ. Chem. J.* **2022**, *5* (04), 5−19.
(57) Aldeen, T. S.; Ahmed Mohamed, H. E.; Maaza, M. ZnO Nanoparticles Prepared via a Green Synthesis Approach: Physical Properties, Photocatalytic and Antibacterial Activity. *J. Phys. Chem. Solids* **2022**, *160*, 110313.
(58) Peerakiatkhajohn, P.; Butburee, T.; Sul, J.-H.; Thaweesak, S.; Yun, J.-H. Efficient and Rapid Photocatalytic Degradation of Methyl Orange Dye Using Al/ZnO Nanoparticles. *Nanomaterials* **2021**, *11* (4), 1059.
(59) Wang, Y.; Yang, C.; Liu, Y.; Fan, Y.; Dang, F.; Qiu, Y.; Zhou, H.; Wang, W.; Liu, Y. Solvothermal Synthesis of ZnO Nanoparticles for Photocatalytic Degradation of Methyl Orange and P-Nitrophenol. *Water* **2021**, *13* (22), 3224.
(60) Khan, I.; Saeed, K.; Zekker, I.; Zhang, B.; Hendi, A. H.; Ahmad, A.; Ahmad, S.; Zada, N.; Ahmad, H.; Shah, L. A.; Shah, T.; Khan, I. Review on Methylene Blue: Its Properties, Uses, Toxicity and Photodegradation. *Water* **2022**, *14* (2), 242.
(61) Zavahir, S.; Elmakki, T.; Ismail, N.; Gulied, M.; Park, H.; Han, D. S. Degradation of Organic Methyl Orange (MO) Dye Using a Photocatalyzed Non-Ferrous Fenton Reaction. *Nanomaterials* **2023**, *13* (4), 639.

https://doi.org/10.1021/acsomega.4c06074
ACS Omega 2025, 10, 9919−9937